HHS Public Access

Author manuscript

Cell Stem Cell. Author manuscript; available in PMC 2021 November 05.

Published in final edited form as:

Cell Stem Cell. 2020 November 05; 27(5): 798–812.e6. doi:10.1016/j.stem.2020.08.005.

Hydrogel network dynamics regulate vascular morphogenesis

Zhao Wei[1,*,&], **Rahel Schnellmann**[1,*], **Hawley C. Pruitt**[1], **Sharon Gerecht**[1,2,3,4,5,^]

[1]Department of Chemical and Biomolecular Engineering, The Institute for NanoBioTechnology, Physical Sciences-Oncology Center, Johns Hopkins University, Baltimore, MD 21218, USA

[2]Department of Materials Science and Engineering, Johns Hopkins University, Baltimore, MD 21218, USA

[3]Department of Biomedical Engineering, Johns Hopkins University School of Medicine, Baltimore, MD, 21205, USA

[4]Department of Oncology, Johns Hopkins University School of Medicine, Baltimore, MD, 21205, USA

[5]Lead Contact

Summary

Matrix dynamics influence how individual cells develop into complex multicellular tissues. Here we have developed hydrogels with identical polymer components but different crosslinking capacities to enable investigation of mechanisms underlying vascular morphogenesis. We show that dynamic (D) hydrogels increase contractility of human endothelial colony forming cells (hECFCs), promote clustering of integrin β1 and the recruitment of vinculin, leading to the activation of focal adhesion kinase (FAK) and metalloproteinase expression. This leads to robust assembly of vasculature and deposition of new basement membrane. We also show that non dynamic (N) hydrogels do not promote FAK signaling, and that stiff D- and N-hydrogels are constrained for vascular morphogenesis. Further, D-hydrogels promote hECFC microvessel formation and angiogenesis in vivo. Our results indicate that cell contractility mediates integrin signaling via inside out signaling and emphasizes the importance of matrix dynamics in vascular tissue formation, thus informing future studies of vascularization and tissue engineering applications.

Graphical Abstract

^Corresponding author: gerecht@jhu.edu.
*Equally contributed to this manuscript
&Current affiliation: The Key Laboratory of Biomedical Information Engineering of Ministry of Education, School of Life Science and Technology, Xi'an Jiaotong University, Xi'an 710049, P.R. China

Author contributions: Z.W., R.S., and S.G. designed the research; Z.W., R.S., and H.C.P. performed the research and analyzed the data; Z. W., R. S., and H.C.P., and S.G. wrote the paper.

Competing interests: The authors declare no competing interests.

Data and materials availability: All data needed to evaluate the conclusions in the paper are present in the paper and/or the Supplementary Materials. Additional data related to this paper may be requested from the authors.

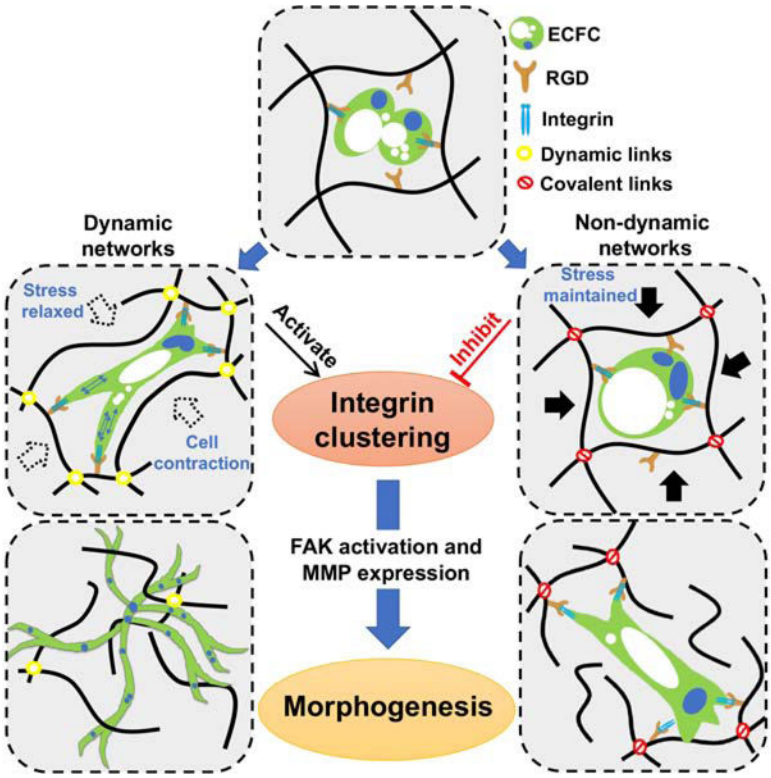

eTOC

Engineered viscoelastic hydrogels with dynamic cross-links permit cell contractility-mediated integrin clustering and FAK activation, independent of hydrogel stiffness, and promote vascular assembly. However, non-dynamic hydrogels prevent cell contractility and integrin clustering, subsequently inhibit the initiation and progression of vascular morphogenesis.

Introduction

Advancements in tissue engineering, aimed at generating complex tissues *in vitro*, are progressing alongside the development of hydrogel materials that mimic aspects of three-dimensional (3D) physiological tissue microenvironments (Discher et al., 2005; Engler et al., 2004; Loebel et al., 2019; Madl et al., 2017; Tang et al., 2018). Vascularization is a critical step in understanding and controlling the assembly of functional healthy tissues (Li et al., 2017; Ronaldson-Bouchard and Vunjak-Novakovic, 2018; Zhang et al., 2016), as well as uncovering the mechanism governing cancer angiogenesis and metastasis via intravasation and extravasation processes (Boussommier-Calleja et al., 2019; Jeon et al., 2015; McCoy et al., 2019).

Mechanosensing has emerged as an important regulator of cellular behaviors, thus impacting the design of hydrogels for tissue engineering. Specifically, it has been well established that secretion of matrix metallopeptidases (MMPs) to allow matrix degradation is a crucial step of vascular morphogenesis (Chun et al., 2004; Davis and Senger, 2005; Iruela-Arispe and Davis, 2009; Sacharidou et al., 2010; Stratman et al., 2009). In agreement, studies focusing

on vascular engineering in hydrogel matrices have shown that progression of vascular morphogenesis occurs alongside decreasing hydrogel stiffness through activation of MMPs (Ghajar et al., 2006; Hanjaya-Putra et al., 2011; Shen et al., 2014; Turturro et al., 2013). For example, West and colleagues developed protease-sensitive poly(ethylene glycol) (PEG) hydrogels with selected moduli for blood vessel formation from human umbilical vein endothelial cells (Moon et al., 2010). The Putnam group engineered another PEG-based hydrogel with MMP-sensitive crosslinkers for capillary morphogenesis from encapsulated ECs (Beamish et al., 2019). Together, these studies have revealed that, with a suitable stiffness, the robust *in vitro* vascular bed could be engineered in the synthetic elastic hydrogels. However, independent of matrix stiffness, recent studies have implicated that viscoelasticity can guide cellular behaviors in hydrogels (Brown et al., 2018; Chang and Chaudhuri, 2019; Lewis et al., 2019; Lou et al., 2018; Nam et al., 2019; Wang and Heilshorn, 2015). Unlike elastic hydrogels, covalently cross-linked viscoelastic hydrogel networks formed with reversible physical interactions or dynamic covalent bonds (de Greef and Meijer, 2008; Wei et al., 2017; Wei et al., 2014; Wojtecki et al., 2011) are able to reconstitute in response to external deformation in a process known as stress relaxation (Carreau, 1972; Matsuoka, 1992). The stress relax performance of these hydrogels has been found consistent with soft tissues and naturally derived extracellular matrix, and thus can be used to better mimic the mechanics of native microenvironments of cells (Chaudhuri et al., 2016; Geerligs et al., 2008; Levental et al., 2007; Liu and Bilston, 2000; McDonald et al., 2009). These dynamic hydrogel networks are able to be remodeled and rearranged in response to the traction forces imposed by the encapsulated cells during culture, allowing the cells to respond in physiologically relevant modes (Huebsch et al., 2010; Swift et al., 2013; Trappmann et al., 2012).

A plethora of strategies have been developed to synthesize hydrogels with stress relaxing behaviors to track the cell behavior and fate including spreading, proliferation, and differentiation of mesenchymal stem cells (MSCs) (Brown et al., 2018; Chaudhuri et al., 2016; Tang et al., 2018), fibroblasts (Chaudhuri et al., 2015), myoblasts (McKinnon et al., 2014), and neural progenitor cells (Madl et al., 2017), as well as the motility and mode of migration of cancer cells (Lewis et al., 2019; Lewis et al., 2017). Nonetheless, studies of how hydrogel network dynamics regulate the assembly of a tissue are scarce. Moreover, while the regulation of the transcriptional regulator YAP (Yes-associated protein) has been documented (Dupont et al., 2011), little is known about the underlying signaling pathways that mediate this mechanosensing process of cellular interactions with hydrogel networks throughout tissue formation.

Here, we hypothesize that dynamic hydrogel networks activate a distinctive mechanosensing-matrix remodeling mechanism that allows vascular tissue assembly. To investigate this, we engineered a viscoelastic hydrogel system by dynamic covalent cross-links that permits vascular tissue assembly, enabling us to determine the role of dynamic networks and the underlying mechanism in regulating vascular tissue morphogenesis. We show that network dynamics enable integrin clustering via increased cell contractility leading to the recruitment of vinculin and the formation of large focal adhesions, thus allowing rapid network formation. Whilst non-dynamic matrices prevent the clustering of integrins and subsequently the initiation and progression of vascular bed formation. We

conclude that matrix dynamics are necessary for integrin clustering and activation highlighting the importance of inside-out signaling through integrin and vascular morphogenesis.

Results

Hydrogels with dynamic and non-dynamic networks

To examine the role of matrix dynamics on tissue assembly, we designed hydrogels from gelatin and dextran, two essential biopolymers commonly used for tissue engineering (Blatchley et al., 2015; Kang et al., 1999; Sun et al., 2010). Gelatin was selected as the main backbone of the hydrogel for its bio-functional cell adhesive motif and cell mediated MMP proteolytic degradable sites on its polymer chains, both required for vascular morphogenesis (Blatchley et al., 2019; Park and Gerecht, 2014; Wei and Gerecht, 2018). We utilized dynamic covalent bonds, imine and acylhydrazone, to generate the dynamic network hydrogel and static covalent bonds of methacrylates to form static, non-dynamic network hydrogels as control (Fig. 1a). For dynamic hydrogel network formation, the gelatin was first modified with adipic acid dihydrazide (ADH) to obtain the Gtn-ADH (Fig. S1a) and the dextran was oxidized to generate multi-aldehyde modified dextran (Dex-CHO) (Fig. 1a). The *in situ* formation of the dynamic hydrogel (D-hydrogel) is achieved by homogeneously mixing Gtn-ADH and Dex-CHO in phosphate-buffered saline (PBS, pH 7.4) under physiological conditions (37°C) with a fixed Gtn-ADH concentration of 5.0 wt%. The imine and acylhydrazone bonds were cross-linked by aldehyde groups on Dex-CHO with the original amino groups and modified acylhydrazide groups on Gtn-ADH, respectively. Known as dynamic covalent bonds, both imine and acylhydrazone have been used for preparation of numerous adaptable and self-healing hydrogels, which can perform intrinsic dynamic equilibrium of bond association and dissociation in polymer networks under physiological conditions (Wei et al., 2015; Wei et al., 2014). Moreover, the acylhydrazone bonds have been shown to be more stable than imine bonds (Wei et al., 2015), and thus can further accelerate the cross-linking efficiency and increase the stability of the dynamic hydrogel networks. Rheological analysis found that the cross-linking point of storage modulus (G') and loss modulus (G''), which presents an estimate of gelation time, occurs much faster in Gtn-ADH than Gtn with the higher final G' (Fig. S1d, e). These data were in concordance with the gelation kinetics observed by phase transition (Fig. S1f), demonstrating that the acylhydrazone bonds induce rapid network formation and enhance the stability of the hydrogels. For the non-dynamic hydrogel (N-hydrogel), methacrylate (MA) modified gelatin (Gtn-MA) (Fig. S1b) and glycidyl MA modified (Dex-GMA) (Fig. S1c) were conventionally cross-linked by UV polymerization in PBS (pH 7.4) to form static covalent hydrogel networks (Fig. 1a). Importantly, the concentrations of the backbones of both hydrogels were kept identical and constant throughout experiments.

We next fabricated D-hydrogels and N-hydrogels with similar initial elastic moduli by adjusting the cross-linker concentration of Dex-CHO (for D-hydrogel) and UV cross-linking time (for N-hydrogel) respectively (stiff or soft; Fig. 1b). To evaluate the rate of stress relaxation profiles of these hydrogels, a constant initial strain was applied in rheological time sweep tests. The resultant relaxation curves were obtained after normalizing the relaxed

stresses to the initial stresses (Fig. 1c). The corresponding relaxation rate was quantified as time of the initial stress to half its original value ($T_{1/2}$). We found that the stress relaxation rates decrease with increasing stiffness of D-hydrogels (Fig. 1d; Fig. S1g–h). In N-hydrogels the relaxation rates are much slower than the D-hydrogels, in both soft and stiff conditions, due to their non-dynamic covalent cross-links. Finally, we immersed the soft D-hydrogels and N-hydrogels in culture media and incubated at 37°C for three days to assess whether their viscoelasticity would be influenced or changed by swelling. As seen in Fig. 1e, there was no significant difference in the G' of both D- and N-hydrogels after 3 days of incubation in media. However, the stress relaxation rates of D-hydrogels decreased with swelling time, (Fig. 1f–g). Nonetheless, the $T_{1/2}$ of D-hydrogels were still significantly shorter than the corresponding N-hydrogels on days 2 and 3, (Fig. 1g), thus providing us a platform to investigate the role of hydrogel network dynamics during vascular morphogenesis.

Hydrogels with dynamic networks promote rapid vascular morphogenesis

Vascular morphogenesis in hydrogels initiates when encapsulated endothelial cells (ECs) engage integrins to interact with the matrix, followed by formation of void spaces termed vacuoles that then coalesce intercellularly and intracellularly to form a lumen (Bayless et al., 2000; Crosby and Zoldan, 2019; Davis and Bayless, 2003; Davis and Camarillo, 1996; Hanjaya-Putra et al., 2011). Sprouting and branching, concurrent with matrix degradation and remodeling, conclude in the formation of a perfusable, nascent vasculature (Davis and Bayless, 2003; Davis and Camarillo, 1996) (Fig. 2a).

Toward generation of vascular bed, we encapsulated human endothelial colony forming cells (ECFCs) in the D-hydrogel and N-hydrogel and examined the kinetics of morphogenesis. Encapsulating ECFCs in the stiffer hydrogels (~600Pa) caused slow progression of vascular morphogenesis (Fig. S2a), corroborating previous works using a variety of hydrogels (Bordeleau et al., 2017; Brown et al., 2020; Hanjaya-Putra et al., 2011; McCoy et al., 2016; Park and Gerecht, 2014; Zheng et al., 2012). Using softer hydrogels (~200Pa), vacuoles could be observed forming in both hydrogels within 4–8 hrs of encapsulation. Interestingly, sprouting and branching were observed in the D-hydrogels on day 1, expanding by day 2 and forming complex vascular bed by day 3 of culture. In contrast, sprouting and branching events were observed in the N-hydrogels only on day 2 following encapsulation and expanding by day 3 (Fig. 2b). We then examined whether the difference in phenotype may be due to different diffusion rates of nutrients and cytokines/growth factors in the two hydrogels. Using Rhodamine B dye, we first confirmed that there is no significant difference in diffusion rates between D- and N-hydrogels (Fig. S2b), demonstrating similar transport properties of the hydrogel networks. To further eliminate the possible concerns of diffusion, both hydrogels were directly prepared with the EGM-2 media. Here too, the ECFCs in D-hydrogels still experienced faster morphogenesis from day 1 to day 3 when compared with N-hydrogels (Fig. S2c).

While multiple studies have demonstrated the safety and cell-based formation of vasculature by UV cross-linked hydrogels (Beamish et al., 2019; Chen et al., 2012; Moon et al., 2010), we carefully examined and compared the cytotoxicity of D-hydrogels and N-hydrogels to eliminate the possible impact on ECFCs. No significant change in cell viability was

observed in samples treated with various gelation precursors of D- and N-hydrogels and UV irradiation, when compared with PBS controls (Fig. S2d). Moreover, Live/Dead staining of ECFCs encapsulated in the D-hydrogel and N-hydrogel for 12 hrs further showed comparable cytocompatibility (78.21% vs. 84.83% respectively, Fig. S2e). Finally, ECFC morphogenesis was found to progress along the 3 days in culture when encapsulated in D-hydrogels with additional Irgacure 2959 and UV irradiation (Fig. S2f).

Examination of vacuole formation in both hydrogels found no significant differences (Fig. S3a,b). Previous works have demonstrated that lumen formation is mediated through activation of the Rho GTPase Cdc42 within 4–24 hrs which is modulated with matrix stiffness (Hanjaya-Putra et al., 2010; Kim et al., 2014). When examining Cdc42 expression, no significant difference was found between the two hydrogels up to 24 hrs (Fig. S3c), suggesting that hydrogel network dynamics do not regulate early stages of vacuole and lumen formation. As vascular morphogenesis progresses with decreasing hydrogel stiffness (Hanjaya-Putra et al., 2011; Shen et al., 2014), we next examined changes in stiffness and stress relaxation along the progression of vasculogenesis. We found that the stiffness of both hydrogels decreased along the culture period, with D-hydrogels becoming significantly softer than N-hydrogels on days 2 and 3 of culture (Fig. 2c), suggesting that the dynamic networks are being degraded as vascular morphogenesis is progressing. Stress relaxation behaviors of both the D-hydrogels and N-hydrogels were not influenced by the encapsulated cells and were consistent with the results of acellular hydrogel incubation in media during the duration of the experiment (Fig. 2d). Finally, we compared the characteristics of the vascular bed formed at the end of the morphogenesis. We found that the dynamic networks enable longer and thicker vessels (tube length and tube volume) as well as the formation of open lumens compared with non-dynamic matrix (Fig. 2e–i). In addition, we found no significant differences in vasculature characteristics between day 3 and 5 of culture following ECFCs encapsulation in D- and N-hydrogels (Fig. S3d,e). Thus, hereafter we focus our analysis on culture periods up to 3 days.

Hydrogels with dynamic networks promote focal adhesion formation and integrin clustering

As no difference was found in the kinetics of vacuoles, we next explored the role of hydrogel networks on cell sprouting and branching, a critical step in the formation of cohesive tissue structures. We hypothesized that the relaxed stress of dynamic networks allows integrins to better engage with hydrogel adhesion motives, such as RGD. The larger network dynamic and stress relaxation of the D-hydrogels further allows efficient formation of initial focal adhesions (FA) and cell contraction leading to the formation of larger integrin clusters. This in turn leads to an increase in integrin signaling and cell contraction and allows cells to deform and remodel the hydrogel networks, thereby enabling efficient sprouting and branching.

To investigate the physical interactions between ECFCs and polymer networks of D-hydrogels or N-hydrogels, 3D traction force microscopy was performed (Legant et al., 2010; Yoon et al., 2019). The fluorescent beads were encapsulated with ECFCs in both D-hydrogel and N-hydrogels, and the displacement and speed of the beads with respect to cells was

analyzed, thus measuring forces applied by ECFCs to the surrounding hydrogel networks. We found that the ECFCs encapsulated in the D-hydrogel deformed the polymer networks more than in the N-hydrogels as indicated by the significantly longer track displacement and higher speed of bead movements during the time lapse (Fig. 3a). To further understand the underlying changes of the differences in traction force, we analyzed phosphorylated myosin light chain (pMLC). We found that cells embedded in D-hydrogels show protrusions and filopodia development within 12 h of culture, with pMLC strongly colocalized to actin (Fig. 3b). However, cells embedded in N-hydrogels didn't show any formation of filopodia nor the development of protrusions and localization of the cells after 12–24 hrs of culture, indicating no ability to migrate within the gel (Fig. 3b, Fig S4a). Additionally, pMLC is mostly localized to the nucleus of the cells embedded in N-gels after 12 hrs of culture with no changes in total pMLC levels in D- and N-hydrogels (Fig. 3b, c). Nuclear localization was not changed after 24 hrs of culture, however the overall amount of pMLC was significantly reduced in cells embedded in N-hydrogels after 24 hrs of culture (Fig.3d). Overall, these results indicate a strong contribution of matrix dynamic in regulation of cell-ECM contacts and cell sprouting.

Focal adhesions are complex structures that localize to sites of cell-matrix interaction through which integrins and scaffold proteins link the actin cytoskeleton to the extracellular matrix (Humphries et al., 2007; Sun et al., 2016). Focal adhesions usually form at filopodia sites and protrusions functioning as adherence points during cell migration. Therefore, we investigated the interaction of integrins with the hydrogel network and whether decrease in traction force has an effect on integrin clustering and FA formation. We found a strong increase in integrin β1 levels and clustering after 24 hrs in culture and significant upregulation of integrin β1 and integrin αV mRNA expression in the D-hydrogels, compared to N-hydrogels (Fig. 3e–g). These results suggest that the dynamic hydrogel networks allow for easier deformation and strong traction forces, which pull on the matrix to a greater extent, facilitating the interaction of integrins with the hydrogel networks followed by integrin clustering.

This clustering of integrin β1 ultimately leads to the recruitment of vinculin (del Rio et al., 2009; Ziegler et al., 2008) and the formation of stable FAs (Fig. 3h, i). The formation of FA in ECFC encapsulated D-hydrogels leads to a remodeling of the cytoskeleton and changes in cell morphology, allowing the ECFCs to spread and initiate sprouting. While ECFCs encapsulated in the N-hydrogel are still capable of vacuole formation, their weak interaction with the matrix and the absence of stable FA results in a static state of ECFCs with no spreading and sprouting (Fig. 3j).

Further analysis of the N- hydrogels and whether there is a delay in timing of vasculogenesis showed that there is moderate increase in integrin β1 expression as well as an increase in filopodia and microspikes after 3 days of culture indicating a delay in integrin clustering (Fig S4b–d), FA formation (Fig S4e) and subsequentially vascular bed progression (Fig. S4f). Nonetheless, the initial delay doesn't allow the cells to "catch up" with robust vascular bed development even after 5 days of culture (see Fig. S3d,e).

Hydrogel network relaxation is necessary for contraction-mediated integrin clustering and subsequent vessel formation

Whether integrin clustering triggers outside-in signaling to facilitate integrin activation or whether clustering occurs after initial activation is still debated. However, certain studies point towards initial integrin FAK activation in an early phase followed by contractility mediated integrin clustering resulting in full FA formation and signaling (Yu et al., 2011).

To further analyze the effect of hydrogel network dynamics on the initiation and progression of vasculogenesis via contractility mediated integrin clustering, we investigated whether inhibition of cell contractility using blebbistatin has a similar effect on integrin clustering as observed in N-hydrogels. As we described above, N-hydrogels do not allow for cell contractility therefore inhibiting the aggregation of distant integrin clusters and stable FA formation (see Fig. 4b). To further investigate this phenomena, we treated ECFCs embedded into D-hydrogels with blebbistatin, a known inhibitor of the myosin-II's ATPase and cell contractility (Kovacs et al., 2004). Inhibition of cell contraction did not impact integrin intensity and number but led to a significant decrease in integrin cluster size and area covered (Fig. 4a, b). These indicate that cell contractility does not regulate initial integrin-RGD binding rather the aggregation and formation of larger integrin clusters. Inhibition of integrin aggregation also led to a decrease in cellular protrusions and filopodia, which is ultimately needed for active cell sprouting and vessel formation (Fig. 4c). Subsequently the formation of the vascular bed was inhibited as shown by shorter tube length and reduced vessel volume in cells treated with blebbistatin for 3 days in D-hydrogels (Fig. 4d).

We conclude that after initial formation of small FAs, cell contractility via pMLC mediated actin contraction promotes integrin clustering, the recruitment of vinculin followed by the activation of downstream signaling events thus promoting downstream signaling and vascular morphogenesis. The non-dynamic matrix however, prevents myosin mediated integrin clustering and therefore does not allow for efficient sprouting and vessel formation. Moreover, matrix rigidity seems to have a significant effect on pMLC localization and translocation to the nucleus as shown in Fig. 3. This effect can't be overcome by cells even after several days in culture.

Dynamic networks lead to the activation of FAK, the upregulation of MMP expression, and new ECM deposition

Previous publications suggest that integrin clustering and activation occurs in several phases, via regulatory signals that originate within the cell cytoplasm and are then transmitted to the external ligand-binding domain of the receptor (Yu et al. 2011). These "inside-out" signals begin with initial integrin binding to RGD sites leads to the recruitment of paxillin and focal adhesion kinase (FAK) in a mechanical force independent manner (Yu et al. 2011) Recruitment of FAK to the FAs leads to its phosphorylation and its consequent activation (Ren et al., 2000; Shi and Boettiger, 2003; Wang and McNiven, 2012). This process is followed by actin polymerization and myosin activation leading to the aggregation of distant integrin clusters and outward translocation (Yu et al., 2011). This process then leads to the recruitment of vinculin and the formation of large stable FAs, resulting in higher cell motility necessary for EC migration during angiogenesis (Hosseini et al., 2019; Pedrosa et

al., 2019). Due to the observed cell contractility mediated integrin clustering and subsequent formation of FAs in the D-hydrogels, we sought to investigate whether FAK is activated in our system and whether it directly contributes to integrin clustering. We found that after 24 hrs post encapsulation, ECFCs cultured in D-hydrogels show significantly higher levels of phosphorylated FAK compared with ECFCs embedded in N-hydrogels (Fig. 5a). However, although ECFCs interact more vigorously with the surrounding matrix in the D-hydrogels through a stronger formation of FAs and activation of FAK, the Yes Associated Protein (YAP) (Fig. S5a) was not localized into the nucleus as previously shown (Tang et al., 2018). This might be contributed to the relatively low stiffness of D- and N-hydrogels (~200 Pa) used for ECFC culture. Taken together these findings suggest that dynamic hydrogel networks can support the formation of FAs and FAK phosphorylation in encapsulated ECFCs.

Further, matrix remodeling and degradation is an important step towards the initiation of vasculogenesis, allowing ECs to invade and vascularize tissues (Davis and Senger, 2005; Iruela-Arispe and Davis, 2009). Specifically, membrane type 1 (MT1)-MMP, MMP1 and MMP9 play major roles in the degradation of the extracellular matrix during angiogenesis (Hanjaya-Putra et al., 2011; Park and Gerecht, 2014). Therefore, we analyzed whether dynamic networks can promote the expression of MMPs in ECFCs. For this, ECFCs were encapsulated in D- and N-hydrogels and cultured for 24 hrs, before the mRNA expression levels were analyzed by qRT-PCR. A significant increase in the expression of MT1-MMP, MMP1 and MMP9 was found in ECFCs encapsulated in D-hydrogels, compared to cells embedded in N-hydrogels (Fig. 5b,c). To further confirm that the ECFC morphogenesis within the D-hydrogels is MMP-dependent, we inhibited MMPs activities using a broad-spectrum inhibitor of MMPs, GM6001 (Blatchley et al., 2019; Hanjaya-Putra et al., 2011). The tubulogenesis of ECFCs in D-hydrogels was inhibited in the presence of GM6001 (0.1 mM) when compared with the controls (Fig. 5d). As we found that the D- hydrogels do not significantly degrade along the culture period in the absence of cells (see Fig 1e above), we examined matrix stiffness following ECFC encapsulation. We found that the D-hydrogels are softer on day 3 of culture (Fig. 5e). When supplementing with MMP inhibitor, GM6001, in the culture media, day 3 hydrogels were found to be significantly stiffer compared with those without MMP inhibitor, further supporting the conclusion that the vascular bed formation in the D-hydrogels is cell-mediated matrix degradation.

As deposition of ECM may contribute to the progression of vascular morphogenesis (Chen et al., 2019; Marchand et al., 2019) we examined expression of collagen IV and laminin, the two major components of the basement membrane deposited by ECs. We found a significant increase of collagen IV and laminin expression in both D- and N-hydrogels along with the culture period (Fig 5f). Interestingly, on day 1 following ECFC encapsulation, the expressions of collagen IV and laminin in D-hydrogels were similar to their expression in the N-hydrogels, while significantly higher in D-hydrogels on day 3. We further found localization of collagen IV in the basement membrane of vessels in D-hydrogel in addition to the formation of large expended inner lumen, both which could not be observed in the N-hydrogels (Fig 5g; Fig. S5b).

These results indicate that the timeline of ECM deposition is longer than the observed phenotype differences occurring at the onset of vasculogenesis. These results further demonstrate that D-hydrogels promote better cell-material interactions, resulting in further remodeling of the matrix that is less prominent in the N-hydrogels.

Collectively, the findings above suggest that the dynamic hydrogel environment facilitates matrix remodeling and degradation, allowing the cells to invade their surroundings and build up vascular tissues.

Activation of FAK regulates integrin clustering, cell contractility, and the subsequent formation of vascular bed

To further delineate the role of FAK signaling and its contribution to integrin clustering and vasculogenesis in D-hydrogels an inhibition study was performed, where FAK phosphorylation was inhibited using the FAK inhibitor FI 14 (Damayanti et al., 2017). ECFCs were embedded in D-hydrogels and subsequently treated with FI 14. The inhibitor-treated constructs showed significant reduction in sprouting (Fig. 6a, b; Fig. S5c,d). Further, analysis of the vasculature revealed that constructs treated with inhibitor had significant reduction in their ability to form vascular bed, as shown by a decrease in tube length and volume (Fig. 6c, d). These findings demonstrate that FAK is not involved in the formation of vacuoles and lumen, however, its activity is key for the progression of vasculogenesis, promoting cell sprouting and subsequent building of vascular tubes and networks.

To determine the contribution of FAK activity to FA formation and stability we analyzed the expression levels of Integrin β1 and Integrin αV mRNA levels in inhibitor treated cells. We found that inhibition of FAK significantly decreases integrin expression, therefore inhibiting the formation of FAs and the progression of vasculogenesis (Fig. 6e). To further analyze the contribution of FAK to integrin clustering, we analyzed the levels and localization of pMLC in D-hydrogels treated with FAK inhibitor for 24 hrs. We found that FAK inhibition doesn't promote localization of pMLC to the nucleus as observed in the N-hydrogel, however FAK inhibition subsequently reduces the phosphorylation of MLC and therefore negatively influences cell contractility and integrin clustering (Fig. 6f).

To further address the function of FAK on cell sprouting and vasculogenesis, we stained the inhibitor treated ECFCs for MT1-MMP expression after 24 hrs in culture. ECFCs treated with FI 14 exhibit significantly lower expression at protein and mRNA levels (Fig. 6g, h). Further analysis of MMP expression showed significant reduction of MMP1 and MMP9 mRNA levels in cells treated with FI 14, compared to untreated controls (Fig. 6h).

Taken together these findings support the hypothesis that FAK is important to maintain and mediate FA stability. Additionally, FAK activation promotes integrin clustering via promotion of MLC phosphorylation and mediation of integrin expression. Further, FAK participates in integrin mediated downstream signaling leading to the upregulation of various MMPs thereby enabling cell sprouting, branching and cell migration necessary for vascular morphogenesis.

In vivo vasculogenic and angiogenic effects of dynamic networks

To determine how dynamic networks impact vascular formation *in vivo*, we examined both vasculogenesis and angiogenesis. For vasculogenesis, pre-prepared GFP-ECFCs-loaded D-hydrogels and N-hydrogels (100 μL for each) were directly implanted subcutaneously in immunodeficient mice (nu/nu mice). Confocal images of GFP-ECFCs in the extracted hydrogel constructs revealed that on both day 3 and day 5, higher cell density with more sprouting and branching cells are present in D-hydrogels compared with N-hydrogels, consistent with our *in vitro* results (Fig. 7a). Low magnification images of histological sections stained for CD31 show that the volume of D-hydrogels are smaller than N-hydrogels on day 3 and day 5, suggesting that D-hydrogels degraded faster than N-hydrogels (Fig. S6abi, i'). High magnification images of those histological sections show numerous $CD31^+$ cells distributed throughout the D-hydrogel on both day 3 and day 5. In contrast, there were fewer $CD31^+$ cells present in the N-hydrogel constructs (Fig. S6abii, ii'). Moreover, the CD31 positive endothelial lining of microvessels can be observed in both D-hydrogel and N-hydrogel constructs (Fig. S9abiii, iii'). Quantification of the density of these $CD31^+$ microvessels revealed more vessels in D-hydrogels compared with N-hydrogels (Fig. S6c). Importantly, on day 7 of transplantation longer sprouts and tubes could be observed (Fig 7a). To further confirm the pathways we identified *in vitro*, we first analyzed pFAK expression in implanted ECFC-loaded D- and N-hydrogels. We found significant increases in FAK activation as indicated by overall intensity of pFAK (Fig 7b). Furthermore, we observed enhanced β1-integrin clustering in D-hydrogels *in vivo* compared to N-hydrogels (Fig 7c). Quantification of pFAK intensity and β1-integrin cluster size confirmed significant increases in D-hydrogels (Fig 7d).

We next examined how hydrogel network dynamics modulate host angiogenesis into the hydrogelin immunocompetent mice (C57BL/6 mice). For this, we transplanted acellular hydrogels with SDF-1α. We chose to use acellular gels to be able to isolate the impact of hydrogel network dynamics on angiogenesis.

As SDF-1 α is secreted following injury to recruit vasculature (Petit et al., 2007; Yamaguchi et al., 2003) we sought to mimic this and examine whether the hydrogel properties, independently of the chemotactic signaling, modulate angiogenic response from the host. After 3 days we could observe cellular infiltration into the D-hydrogel with perfused vasculature at the edge of the hydrogel while very little cells could be observed penetrating the N-hydrogel (Fig 7e; Fig S7a). To further demonstrate functionality of the infiltrating vessels, Evan's blue dye was injected intravenously prior to explanation of acellular gels on day 3. *In situ* confocal imaging shows perfused vessels, stained with lectin, within the D-hydrogel (Fig 7c, Fig S7b,c). Overall, these results suggest that the dynamic networks facilitate rapid vasculogenesis *in vivo*, as well as host angiogenesis and circulation further extending the observation to applications of vascular regeneration.

Discussion

Defining the mechanism for fast vasculogenesis driven by dynamic hydrogel networks

Studies have begun to explore the role of dynamics of hydrogels during cell differentiation and migration. However, assembly of a tissue requires a coordinated sequence of events to occur in a temporal and spatial manner in neighboring cells. Specifically, in vascular morphogenesis, endothelial cells undergo vacuolization followed by synchronized sprouting and branching events, forming complex bed of tubular structures (Bayless et al., 2000; Crosby and Zoldan, 2019; Davis and Bayless, 2003; Davis and Camarillo, 1996; Davis and Senger, 2005; Iruela-Arispe and Davis, 2009). This process initiates with rapid matrix-integrin binding and proceeds with matrix degradation. To identify and understand the role of stress relaxation in this process, a tailored hydrogel system was required that not only decouples hydrogel network dynamics from other physical properties, mainly stiffness, but allows the process of tissue assembly to progress. By using our gelatin/dextran-based D-hydrogel and N-hydrogel systems, we show that the stress relaxation of dynamic hydrogel networks, independent of stiffness, promote the interaction of cell surface integrin with the RGD sites of the matrix. The initial integrin–RGD interactions then lead to the recruitment of FAK and other adaptor proteins such as talin (del Rio et al., 2009; Tadokoro et al., 2003) and paxillin (Brown et al., 1996; Mofrad et al., 2004) in a non-stiffness and mechano-sensitive manner. Following this first step of FA formation, pMLC localization to the actin cytoskeleton and actin contraction then leads to the aggregation of distant integrin clusters and the formation of larger FAs with recruitment of vinculin and further FAK activation. Activated FAK then further contributes to the phosphorylation of MLC and integrin expression, therefore supporting the formation of larger integrin clusters. Thus, FAK is a key mediator in integrin clustering, stable FA formation and downstream signaling necessary for cell migration and vessel formation.

FAK mediated downstream signaling leads to an increase in MT1-MMP, MMP9 and MMP1 expression, which leads to the degradation and subsequent remodeling of the matrix, allowing the cells to sprout, branch, and ultimately form expansive vascular bed (Fig. 7g). Matrix network dynamics is hereby a key mediator of vascular tissue assembly. A non-dynamic matrix prevents contraction-mediated integrin clustering leading to the abrogation of cell signaling, which ultimately leads to the inhibition of vascular morphogenesis.

Vascularization is a key process that enable engineering of tissues, either healthy or cancerous. The implications of these results serve not only towards understanding how hydrogel network dynamics influence vascular morphogenesis, but as a framework for designing hydrogel biomaterials that can be applied to studying complex tissue assembly and morphogenesis, and towards range of therapeutics.

Limitations of the Study

Cell mediated remodeling of the matrix is an essential process during vascular morphogenesis, thus altering the mechanical properties of the hydrogel system. As a result, our investigations are limited to short term studies in which we can study the direct effect of matrix dynamics on the initiation of vasculogenesis. *In vitro*, by day 3 of culture we

observed cell-mediated degradation and new basement membrane deposition. *In vivo*, by day 3 we show rapid invasion of vessel into the cell free hydrogels as well as the formation of microvessels in the cell laden gels. Due to the fast degradation of the dynamic hydrogel by cells, the *in vivo* studies were limited to up to 7 days.

STAR Methods

Resource Availability

Lead Contact—Further information and requests for resources should be directed to and will be fulfilled by the Lead Contact, Sharon Gerecht (Gerecht@jhu.edu).

Materials availability—This study did not generate new unique reagents.

Data and Code Availability—This study did not generate/analyze datasets/code.

EXPERIMENTAL MODEL AND SUBJECT DETAILS

GFP-ECFCs cell lines—Primary human endothelial colony forming cells (ECFCs) were a gift from M.Yoder (Indiana University) and GFP-expressing primary human ECFCs (GFP-ECFCs) were generated and provided by K.Eisinger (University of Pennsylvania), following previously described protocol (Eisinger-Mathason et al., 2013)). Cells were maintained as previously described (Blatchley et al., 2019). In brief, cells were cultured on collagen type I (BD Biosciences) coated dishes in endothelial growth media (EGM 2, Lonza) media containing 10% FBS (Hyclone) and VEGF (R&D Systems) with media changes every other day. When cells reached confluency they were incubated with 0.5% Trypsin/EDTA solution (ThermoFisher Scientific) until fully detached. Cells were collected in culture medium, centrifuged and either embedded into hydrogels for further experiments or expanded on colIagen type I culture flasks. For all experiments cells were used between passages 6–9.

In vivo studies—The 7–8 weeks old female nude mice (Charles River) and 6–8 week old C57BL/6 male mice (The Jackson Laboratory) were used for the in vivo studies. Mice were kept under specific pathogen-free conditions in the medical school of Johns Hopkins University, Division of Animal Resources. They were housed with a maximum of 5 mice per cage prior to the experiments. Mice were randomly grouped for subsequent subcutaneous experiments. All animal procedures complied with the NIH Guidelines for the Care and Use of Laboratory Animals and were approved by the Institutional Animal Care and Use Committee.

METHOD DETAILS

Synthesis of Gtn-ADH and Dex-CHO—Gtn-ADH was synthesized as in previous protocol with modifications (Hozumi et al., 2018). 1.0 g of gelatin (Type A; Sigma-Aldrich) was dissolved in 40 mL of PBS (pH 5.5), and added with 1.74 g, 10 mmol of Adipic acid dihydrazide (ADH;> 98.0%; Sigma-Aldrich) at 50°C with stirring. Next, 0.77 g, 5.7 mmol of 1-Hydroxybenzotriazole hydrate (HOBt;≥ 97.0%; Adipic acid dihydrazide) dissolved in 5 mL of DMSO (Sigma-Aldrich) was added to the mixture. Then 0.77 g, 4.0 mmol of N-(3-Dimethylaminopropyl)-N’-ethylcarbodiimide hydrochloride (EDC; Sigma-Aldrich)

(Crystalline) was directly added to the mixture, and the pH was adjusted to 5.0–5.3 by using 1 M of NaOH. The mixture was stirred overnight at 50°C and the solution became bright yellow. The product was purified by dialysis (MWCO 8000) against distilled water for a week with the water changed every day, followed by lyophilization to obtain Gtn-ADH. The new proton peaks, at 1.7 ppm and 2.5 ppm, indicated the coupling of ADH on the gelatin chains from the ^{1}H NMR spectra (Fig. S1a), which was recorded in D_2O on a 400 MHz Spectrometer (Bruker Avance). The degree of modification was evaluated by trinitrobenzene sulfonic acid (TNBS, 5.0% w/v) assay described previously (Freedman and Radda, 1968). This assay indicates that 32.7% of carboxy groups were substituted with hydrazide groups under the reacted conditions in this study. Dex-CHO was synthesized as reported previously with a slight modification (Wei and Gerecht, 2018). In brief, 1.0 g, 6.2 mmol of dextran (Mn = 110,000; Sigma-Aldrich) was dissolved in 100 mL of distilled water, and then sodium periodate (> 99.0%; Sigma-Aldrich) (1.0 g, 4.6 mmol) in 1 mL of distilled water was added dropwise. The solution was stirred in the dark for 20 min. The oxidation reaction was terminated by adding 1.0 mL ethylene glycol and stirring for an additional 30 min. The mixture was then dialyzed (MWCO 3500) against distilled water for a week with the water changed every day, followed by lyophilization to obtain Dex-CHO. The oxidation percentage of Dex-CHO was ~22.8%, which was determined by quantifying the number of aldehyde groups in the polymer using tert-butylcarbazate (t-BC, > 98.0%; Sigma-Aldrich) as described previously (Maia et al., 2005). The aldehyde groups of Dex-CHO reacted with carbazates of t-BC (excess amount) to form carbazones, subsequently the unreacted t-BC was quantified by adding TNBS. The resulting colored trinitrophenyl-derivative was measured at 334 nm using a spectrophotometer.

Synthesis of Gtn-MA and Dex-MA—The Gtn-MA was synthesized using the approaches previously described, with slight modification (Zhao et al., 2016). In brief, 1.0 g of gelatin was dissolved in 100 mL of PBS (pH 7.4) at 60°C, and 8.0 mL of methacrylic anhydride (94.0%; Sigma-Aldrich) was added in the solution, stirring for 3 hrs at 50°C. The product was finally dialyzed at 40°C (MWCO 8000) against distilled water for a week with the water changed every day, followed by lyophilization to obtain Gtn-MA. The degree of methacrylation was determined as 78.1% from ^{1}H NMR spectra by integrating peaks at 7.3 ppm and peaks at 5.4 ppm and 5.7 ppm, which were corresponded to the aromatic residues of gelatin and methacrylamides, respectively (Fig. S1c). ^{1}H NMR spectra were recorded in D_2O on a 400 MHz Spectrometer. The synthesis of Dex-MA was conducted as previously reported (Liu et al., 2015). Briefly, 1.0 g, 6.2 mmol of dextran was dissolved in 40 mL of DMSO and then 0.19 g, 1.55 mmol of 4-dimethylaminopyridine (DMAP, ≥ 99.0% Sigma-Aldrich) and 0.44 g, 3.1 mmol of glycidyl methacrylate (GMA, 97.0%; Sigma-Aldrich) were added to the solution. The mixture was stirred at 50°C overnight and an equimolar amount of HCl was added to neutralize the DMAP. The product was purified by dialysis (MWCO 8000) against distilled water for a week with the water changed every day, followed by lyophilization to obtain Dex-MA. The degree of substitution was calculated as 34.0% from ^{1}H NMR spectra by comparing the ratio of the areas under the proton peaks at 6.2 ppm and 5.3 ppm to the peak at 4.8 ppm (Fig. S1c). ^{1}H NMR spectra were recorded in D_2O on a 400 MHz Spectrometer.

Preparation of the D-hydrogels and N-hydrogels—For the D-hydrogel formation, the Gtn-ADH and Dex-CHO were dissolved into PBS (pH 7.4) respectively. The solutions were mixed uniformly by pipette and then placed in 37°C water bath or incubator. The transparent D-hydrogel was formed after several minutes. The total weight concentration of Gtn-ADH was kept as a constant of 5 wt% and the final weight concentration of Dex-CHO was kept as 0.5 wt% (stiff gel) or 0.25 wt% (soft gel). For the N-hydrogel formation, the PBS (pH 7.4) of Gtn-MA, Dex-MA and the photoinitiator 2-hydroxy-4'-(2-hydroxyethoxy)-2-methylpropiophenone (Irgacure 2959; Sigma-Aldrich) were mixed uniformly by pipette. The N-hydrogel was obtained by UV polymerization of 50 s (stiff gel) or 20 s (soft gel). The concentration of initiator 2959 was kept at a constant of 0.5 wt%. The weight concentrations of the Gtn-MA and Dex-MA were kept identical with the corresponding D-hydrogels.

Rheological measurements—The mechanical properties of the hydrogels were tested by a rheometer (AR-G2, TA instruments) equipped with 25 mm or 8 mm parallel plate at 37°C. In the gelation experiments of D-hydrogels, the hydrogel precursor solutions were mixed on the bottom plate in the instrument. The dynamic time sweeps were performed on the D-hydrogel samples in soft and stiff conditions respectively by using 25 mm plate. The G' and G'' were monitored at a fixed strain of 0.1% and a fixed frequency of 1 Hz. The G' of the well-formed D-hydrogels and N-hydrogels were also tested on this rheometer, equipped with 8 mm parallel plates at 37°C. All the D-hydrogels and N-hydrogels with various conditions were prepared as discs measuring 8 mm in diameter. At a fixed strain of 0.1%, the frequency sweep was performed on the samples and the data was collected from the platform region. A solvent trap wetted with PBS was used to prevent sample dehydration during the measurements. Moreover, the G' of D-hydrogel and N-hydrogel encapsulated with ECFCs were also tested, at different time points along with the increased culture time, by the same method. In addition, stress relaxation measurements of both D-hydrogel and N-hydrogel were performed by time sweep tests at a constant initial strain of 10% and a fixed frequency of 1 Hz. The corresponding stress relaxation curves were then normalized to their initial value and fitted to a stretched exponential function as $\sigma/\sigma_0 = e^{-(t/\mathrm{Tk})\beta}$ as previously reported (Fig. S3) (Brown et al., 2018), where σ/σ_0 is the normalized stress, T_k is the fitted time constant and β ($0 < \beta < 1$) is the stretching exponent. The t is the experiment time and the fitting were performed in Matlab. The relaxation rate was quantified as the time for the initial stress to half of its original value as $T_{1/2}$ throughout the paper.

Diffusion tests of D-hydrogels and N-hydrogels—The softer D-hydrogels and N-hydrogels were immersed in the Rhodamine B (1.0 mg L^{-1} in PBS; Sigma-Aldrich) at 37°C, then taken out at selected time points and inserted into the vials. 1 mL collagenase IV (0.05%) was added to each hydrogel for proteolytic degradation. After 30 min by which time point the hydrogels were fully degraded, the absorbance of each sample was measure using a microplate reader at a wavelength of 554 nm. D- and N-hydrogels in collagenase IV solution were set as the controls/blanks.

Encapsulation of ECFCs in D-hydrogels and N-hydrogels—To encapsulate cells in D-hydrogel, the Gtn-ADH and Dex-CHO were dissolved into PBS (pH 7.4) respectively.

The cell pellet was mixed with the Dex-CHO solution and VEGF (R&D Systems; 50 ng mL^{-1}) and bFGF (R&D Systems; 50 ng mL^{-1}) to obtain a cell suspension at a concentration of 4×10^{6} cell mL^{-1}. The Gtn-ADH solution was then added to this cell mixture and pipetted homogeneously. The mixture of 90 μL totally was transferred into a PDMS mold with 8 mm diameters and placed into the incubator for 30 min of gelation, before adding 1 mL of EGM-2 (Lonza) with 10% FBS (Hyclone), VEGF (R&D Systems; 50 ng mL^{-1}) and bFGF (R&D Systems; 50 ng mL^{-1}) (Stratman et al., 2011). The media was replaced every 24 hrs. To encapsulate cells in N-hydrogel control, the cell pellet was mixed with the Gtn-MA, Dex-MA and Irgacure 2959 uniformly mixed by pipette with PBS (pH 7.4) with VEGF (R&D Systems; 50 ng mL^{-1}) and bFGF (R&D Systems; 50 ng mL^{-1}) to obtain a cell suspension at a concentration of 4×10^{6} cell mL^{-1}, which was then transferred into the PDMS mold with 8 mm diameters. The hydrogels were obtained by UV polymerization, then adding 1 mL of EGM-2 (Lonza) with 10% FBS (Hyclone) with VEGF (R&D Systems; 50 ng mL^{-1}) and bFGF (R&D Systems; 50 ng mL^{-1}) with replacement of every 24 hrs. The morphologies of the encapsulated ECFCs were observed and tracked by optical microscopy (phase-contrast) and confocal microscopy (LSM 780, Zeiss).

Cytocompatibility of D-hydrogel and N-hydrogel components—The cytotoxicity was investigated by WST-1 assay (Roche) according to the manufacturer's instructions. In brief, 2×10^{4} cells were cultured in 100 mL EGM-2 media (Lonza) with 10% FBS (Hyclone) in each well of 96-well plate and treated by Gtn-MA (5 wt%), Gtn-ADH (5 wt%), Dex-MA (0.5 wt%), Dex-CHO (0.5 wt%), Irgacure 2959 (0.5 wt%) and 50 s UV, respectively. PBS only, Gtn and Dex were set as controls. After 24 hrs incubation, 10 μL of WST-1 mixture was added to each well. After placing in an incubator for another 2 hrs, the absorbance of each sample was measured using a microplate reader at a wavelength of 450 nm. Cell viability was determined as the percentage of PBS controls.

Traction force microscopy—D-hydrogel and N-hydrogel precursor solutions were prepared as stated above. 1 μm FluoSpheres (ThermoFisher Scientific) that are carboxylated were rinsed with PBS 2 times and then mixed with the GFP-ECFC pellet prior to hydrogel formation. We have chosen 1μm beads as they are large enough to neglect Brownian displacements (Bloom et al., 2008). Using a confocal microscope (LSM 780, Zeiss) z-stacks of beads were taken in 1 min intervals for 20 min to observe bead movement, according to a previously established method (Bloom et al., 2008).

Fak-specific inhibition (FI 14), MMP inhibition (GM6001), and blebbistatin inhibition studies—For 2D screening of the FI 14 (FI-14, ≥ 95.0%; Sigma-Aldrich), the ECFCs were seeded into a 96-well plate at a cell density of 10000 cells/well in EGM-2 media (Lonza) with 10% FBS (Hyclone). After 1 day of culture, 100 μL of EGM-2 media containing increased concentrations of FI 14 ranging from 0 to 10 μM were added per well and culture for additional 24 hrs following by staining for phospho-FAK (Tyr397;ThermoFisher Scientific) as described below. Biological triplicates were tested for each FI 14 concentrations. For inhibition studies, ECFCs were suspended in the hydrogel precursor as above with the addition of 10 μM of FI-14 (Sigma-Aldrich) or GM6001 (1 mg mL$^{-1;}$ Sigma-Aldrich), 60 μM Blebbistain (Sigma-Aldrich) or vehicle control (DMSO;

Sigma-Aldrich). The corresponding culture media also supplied with the corresponding inhibitor/vehicle control at the same concentration. Media was replenish every 24 h till analysis.

Vacuole visualization and quantification—Quantification of vacuoles and lumen formation in 4–8 hrs was performed using light microscopy as previously reported (Bayless et al., 2000). For each D-hydrogel and N-hydrogel condition, we analyzed biological triplicates with 2–3 images per replicate for vacuole and lumen formation. A cell was considered to be vacuolating if > 30% of the cell's area contained a vacuole or lumen.

Immunofluorescence (IF)—The D-hydrogel or N-hydrogel constructs were fixed with 2% paraformaldehyde (PFA; Sigma-Aldrich) for 20 min at room temperature, then washed three times with PBS with 10 min in between each wash. For staining, the encapsulated cells were permeabilized with a solution of 0.5% Triton-X (Sigma-Aldrich) for 20 min, followed by staining with primary antibody in antibody diluent solution (Life Technologies; 1:100) overnight at 4°C, then washed with PBS three times with 10 min in between each wash. Hydrogels were then incubated in a secondary antibody in antibody diluent solution (Life Technologies; 1:250) for 4 hours at room temperature and then washed with PBS three times with 10 min between each wash. Finally, the hydrogels were counterstained with DAPI (ThermoFisher Scientific; 1:1000) for 15 min at room temperature and then washed with PBS with 10 min in between each wash before analyzing using confocal microscopy. Primary antibodies of anti-Cdc42 (clone 11A1; Cell Signaling), anti-Integrin β1 (clone 4Br7; Santa Cruz Biotechnology, anti-Vinculin (Sigma-Aldrich), anti-phospho-FAK (Tyr397; ThermoFisher Scientific), anti-MMP14 (clone EP1264Y; abcam), anti-YAP (clone H-125; Santa Cruz Biotechnology), anti ColIV (abcam), anti-pMLC (Cell Signaling) were diluted in antibody diluent as 1:100, according to the manufacturer's protocol. Secondary antibodies of goat 488/546 (Invitrogen) or mouse 488/546 (Invitrogen) with 635 phalloidin (Invitrogen) were used at 1:250 in antibody diluent. Images were taken using fluorescence (AxioObserver Zeiss) or confocal (LSM 780 or LSM 800, Zeiss) microscopes. To image lumen, orthogonal views (z-stacks) where taken and merged to the corresponding plain views (x,y, stacks) in the figure. For IF-based quantification, the intensity of Cdc42, integrin β1 and p-FAK were normalized to the intensity of corresponding DAPI using ImageJ. Biological triplicates (10 cells per replicate, 30 cells total) in each condition were used for the analysis. The aspect ratio was also obtained by ImageJ from IF images of actin with biological triplicates (20 cells per replicate, 60 cells total). The analysis of FA and integrin cluster size, number and areas were performed by ImageJ as shown in previous publication (Humphries et al., 2007). Biological triplicates (10 cells per replicate, 30 cells totally) in each condition were used for this analysis. The quantification of vascular tube length and tube volume in D-hydrogel and N-hydrogel were analyzed using Imaris. Biological triplicates with 5–6 images per replicate were used for the analysis.

For nuclear protein quantification the images were analyzed using ImageJ software. The z stacks were analyzed using average intensity z-projections. DAPI staining was used to outline the nucleus and the nuclear pMLC signal intensity was normalized to overall pMLC intensity.

Real-time RT-PCR—Quantitative real time RT-PCR was performed as described previously (Hanjaya-Putra et al., 2011; Park and Gerecht, 2014). In brief, total RNA was isolated from ECFCs encapsulated in D-hydrogels or N-hydrogels using TRIzol according to the manufacturer's instructions. Two-step RT-PCR was performed using TaqMan™ Gene Expression Master Mix (ThermoFisher Scientific) according to the manufacturer's instructions: for MT1-MMP ((hs01037003_g1), Integrin β1 (hs00559595_m1), Integrin α5 (hs00233808_m1), MMP1 (hs00233958_m1), MMP9 (hs00957562_m1), Collagen IV (hs00266237_m1) and laminin (hs00267056_m; all from ThermoFisher Scientific). All samples were examined in triplicate, analyzed, and graphed as previously described (Hanjaya-Putra et al., 2011; Park and Gerecht, 2014).

***In vivo* subcutaneous implantation of GFP-ECFC-loaded D-hydrogels and N-hydrogels—**To analyze *in vivo* vasculogenesis, the ECFCs or GFP-ECFC-loaded D- and N-hydrogels (pre-prepared as detailed above) were subcutaneously implanted into nude mice (7–8 week-old females; N = 3) as in previous studies (Ghajar et al., 2006; Wei and Gerecht, 2018). To analyze vascularization of acellular hydrogel constructs (ie angiogenesis), gels were subcutaneously implanted in C57Bl/6J mice (6–8 week-old males; N=3 per group). In both cases, the constructs were subcutaneously implanted and sutured into both flanks of the mice (100 μL of each side). To assess perfused vessels in the gel, Evans blue dye (Sigma-Aldrich) at 30 mg/kg; 150 μL in PBS was injected into the lateral tail vein prior to euthanasia. At each time point indicated, mice were euthanized and the constructs were removed with surrounding tissue, fixed in 3.7% PFA (Sigma-Aldrich). The explants were immediately analyzed using *in situ* confocal imaging and then proceeded to histological analysis. The animal studies were performed using a protocol # MO19E328 approved by The Johns Hopkins University Institutional Animal Care and Use Committee.

Immunohistochemistry—For immunohistochemical analysis, paraffin embedded tissue sections (5 μm) were dehydrated through graded ethanol followed by heat mediated antigen retrieval and incubation of anti-CD31 (abcam; 1:500), anti-phospho-FAK (ThermoFisher Scientific; 1:200), and anti-integrin-β1 (Santa Cruz Biotechnology; 1:200) diluted in antibody diluent overnight at 4°C. For CD31 staining the ImmPRESS HRP anti-rabbit IgG polymer detection kit (Vector Laboratories) and DAB was used for detection followed by counterstaining with hematoxylin. Quantification was performed by ImageJ to count $CD31^+$ positive cells and microvessels. For immunofluorescent detection of phospho-FAK and Integrin-β1 anti-rabbit IgG secondary antibody Alexa Fluor 546 conjugate (Invitrogen; 1:500) and anti-mouse IgG secondary antibody Alexa Fluor 546 conjugate (Invitrogen;1:500) were used. Slides were counterstained with DAPI (ThermoFisher Scientific; 1:1000). Quantification of overall expression was performed using ImageJ by calculating the integrated density of the signal for each cell.

QUANTIFICATION AND STATISTICAL ANALYSIS

Characterization of hydrogels, including stiffness, stress relaxation, cytocompatibility, and diffusion rates, were performed in N = 3 (biological replicates) with technical duplicates; image based quantifications were performed in at least N = 3 biological samples in technical duplicates and detailed throughout the methods and figure legends; qRT-PCR was performed

in N = 3 biological samples with technical triplicate. Analysis of stress relaxation of the hydrogel was performed using a custom MATLAB script. Analysis of cell aspects, fluorescence intensity and FA measurements were performed using ImageJ. The filaments of vascular networks in the hydrogels were quantified using Imaris. The statistical analysis was performed by GraphPad Prism 6. We also used this software to perform t-tests to determine significance. All graphical data are reported as means ± SD. Significance levels were set at $*P < 0.05$, $**P < 0.01$, $***P < 0.001$, and $****P < 0.0001$. All graphical data were reported.

Supplementary Material

Refer to Web version on PubMed Central for supplementary material.

Acknowledgments

We would like to thank Christine Duke for editing the manuscript and Dr. Chongpu Zhai for helping with matlab analysis. We thank M. Yoder for the ECFCs and K. Eisinger and K. Pak for transfection of GFP-ECFCs. This work was supported by a fellowship from the Maryland Stem Cell Fund (MSCRFF-3928 to Z.W; MSCRFF-5159 to RS), fellowship from the Nanotechnology for Cancer Research Training Grant 5T32CA153952-09 (to HCP), the NCI Physical Sciences-Oncology Center (U54CA210173), MSCRFI-2784 from Maryland Stem Cells Research Fund, and 15EIA22530000 from American Heart Association (to S. Gerecht). The authors acknowledge services provided by the Johns Hopkins University Oncology Tissue Services core Sydney Kimmel Cancer Center (P30 CA006973) as well as the Johns Hopkins University Integrated Imaging Center.

References

Bayless KJ, Salazar R, and Davis GE (2000). RGD-dependent vacuolation and lumen formation observed during endothelial cell morphogenesis in three-dimensional fibrin matrices involves the αvβ3 and α5β1 integrins. The American journal of pathology 156, 1673–1683. [PubMed: 10793078]

Beamish JA, Juliar BA, Cleveland DS, Busch ME, Nimmagadda L, and Putnam AJ (2019). Deciphering the relative roles of matrix metalloproteinase-and plasmin-mediated matrix degradation during capillary morphogenesis using engineered hydrogels. Journal of Biomedical Materials Research Part B: Applied Biomaterials.

Blatchley M, Park KM, and Gerecht S (2015). Designer hydrogels for precision control of oxygen tension and mechanical properties. Journal of Materials Chemistry B 3, 7939–7949. [PubMed: 26693017]

Blatchley MR, Hall F, Wang S, Pruitt HC, and Gerecht S (2019). Hypoxia and matrix viscoelasticity sequentially regulate endothelial progenitor cluster-based vasculogenesis. Science advances 5, eaau7518. [PubMed: 30906859]

Bloom RJ, George JP, Celedon A, Sun SX, and Wirtz D (2008). Mapping local matrix remodeling induced by a migrating tumor cell using three-dimensional multiple-particle tracking. Biophysical journal 95, 4077–4088. [PubMed: 18641063]

Bordeleau F, Mason BN, Lollis EM, Mazzola M, Zanotelli MR, Somasegar S, Califano JP, Montague C, LaValley DJ, and Huynh J (2017). Matrix stiffening promotes a tumor vasculature phenotype. Proceedings of the National Academy of Sciences 114, 492–497.

Boussommier-Calleja A, Atiyas Y, Haase K, Headley M, Lewis C, and Kamm R (2019). The effects of monocytes on tumor cell extravasation in a 3D vascularized microfluidic model. Biomaterials 198, 180–193. [PubMed: 29548546]

Brown A, He H, Trumper E, Valdez J, Hammond P, and Griffith LG (2020). Engineering PEG-based hydrogels to foster efficient endothelial network formation in free-swelling and confined microenvironments. Biomaterials 243, 119921. [PubMed: 32172030]

Brown MC, Perrotta JA, and Turner CE (1996). Identification of LIM3 as the principal determinant of paxillin focal adhesion localization and characterization of a novel motif on paxillin directing

vinculin and focal adhesion kinase binding. The Journal of cell biology 135, 1109–1123. [PubMed: 8922390]

Brown TE, Carberry BJ, Worrell BT, Dudaryeva OY, McBride MK, Bowman CN, and Anseth KS (2018). Photopolymerized dynamic hydrogels with tunable viscoelastic properties through thioester exchange. Biomaterials 178, 496–503. [PubMed: 29653871]

Carreau PJ (1972). Rheological equations from molecular network theories. Transactions of the Society of Rheology 16, 99–127.

Chang J, and Chaudhuri O (2019). Beyond proteases: Basement membrane mechanics and cancer invasion. The Journal of cell biology 218, 2456–2469. [PubMed: 31315943]

Chaudhuri O, Gu L, Darnell M, Klumpers D, Bencherif SA, Weaver JC, Huebsch N, and Mooney DJ (2015). Substrate stress relaxation regulates cell spreading. Nature communications 6, 6365.

Chaudhuri O, Gu L, Klumpers D, Darnell M, Bencherif SA, Weaver JC, Huebsch N, Lee H. p., Lippens E, and Duda GN (2016). Hydrogels with tunable stress relaxation regulate stem cell fate and activity. Nature materials 15, 326. [PubMed: 26618884]

Chen D, Teng JM, North PE, Lapinski PE, and King PD (2019). RASA1-dependent cellular export of collagen IV controls blood and lymphatic vascular development. J Clin Invest 129, 3545–3561. [PubMed: 31185000]

Chen YC, Lin RZ, Qi H, Yang Y, Bae H, Melero-Martin JM, and Khademhosseini A (2012). Functional human vascular network generated in photocrosslinkable gelatin methacrylate hydrogels. Advanced functional materials 22, 2027–2039. [PubMed: 22907987]

Chun T-H, Sabeh F, Ota I, Murphy H, McDonagh KT, Holmbeck K, Birkedal-Hansen H, Allen ED, and Weiss SJ (2004). MT1-MMP–dependent neovessel formation within the confines of the three-dimensional extracellular matrix. J Cell Biol 167, 757–767. [PubMed: 15545316]

Crosby CO, and Zoldan J (2019). Mimicking the physical cues of the ECM in angiogenic biomaterials. Regenerative biomaterials 6, 61–73. [PubMed: 30967961]

Damayanti NP, Buno K, Narayanan N, Harbin SLV, Deng M, and Irudayaraj JM (2017). Monitoring focal adhesion kinase phosphorylation dynamics in live cells. Analyst 142, 2713–2716. [PubMed: 28589989]

Davis GE, and Bayless KJ (2003). An integrin and Rho GTPase-dependent pinocytic vacuole mechanism controls capillary lumen formation in collagen and fibrin matrices. Microcirculation 10, 27–44. [PubMed: 12610662]

Davis GE, and Camarillo CW (1996). An α.2β1 integrin-dependent pinocytic mechanism involving intracellular vacuole formation and coalescence regulates capillary lumen and tube formation in three-dimensional collagen matrix. Experimental cell research 224, 39–51. [PubMed: 8612690]

Davis GE, and Senger DR (2005). Endothelial extracellular matrix: biosynthesis, remodeling, and functions during vascular morphogenesis and neovessel stabilization. Circulation research 97, 1093–1107. [PubMed: 16306453]

de Greef TF, and Meijer E (2008). Materials science: Supramolecular polymers. Nature 453, 171. [PubMed: 18464733]

del Rio A, Perez-Jimenez R, Liu R, Roca-Cusachs P, Fernandez JM, and Sheetz MP (2009). Stretching single talin rod molecules activates vinculin binding. Science 323, 638–641. [PubMed: 19179532]

Discher DE, Janmey P, and Wang Y. l. (2005). Tissue cells feel and respond to the stiffness of their substrate. Science 310, 1139–1143. [PubMed: 16293750]

Dupont S, Morsut L, Aragona M, Enzo E, Giulitti S, Cordenonsi M, Zanconato F, Le Digabel J, Forcato M, and Bicciato S (2011). Role of YAP/TAZ in mechanotransduction. Nature 474, 179. [PubMed: 21654799]

Eisinger-Mathason TS, Zhang M, Qiu Q, Skuli N, Nakazawa MS, Karakasheva T, Mucaj V, Shay JE, Stangenberg L, Sadri N, et al. (2013). Hypoxia-dependent modification of collagen networks promotes sarcoma metastasis. Cancer Discov 3, 1190–1205. [PubMed: 23906982]

Engler AJ, Griffin MA, Sen S, Bönnemann CG, Sweeney HL, and Discher DE (2004). Myotubes differentiate optimally on substrates with tissue-like stiffness: pathological implications for soft or stiff microenvironments. J Cell Biol 166, 877–887. [PubMed: 15364962]

Freedman R, and Radda G (1968). The reaction of 2, 4, 6-trinitrobenzenesulphonic acid with amino acids, peptides and proteins. Biochemical Journal 108, 383–391. [PubMed: 5667253]

Geerligs M, Peters GW, Ackermans PA, Oomens CW, and Baaijens F (2008). Linear viscoelastic behavior of subcutaneous adipose tissue. Biorheology 45, 677–688. [PubMed: 19065014]

Ghajar CM, Blevins KS, Hughes CC, George SC, and Putnam AJ (2006). Mesenchymal stem cells enhance angiogenesis in mechanically viable prevascularized tissues via early matrix metalloproteinase upregulation. Tissue engineering 12, 2875–2888. [PubMed: 17518656]

Hanjaya-Putra D, Bose V, Shen Y-I, Yee J, Khetan S, Fox-Talbot K, Steenbergen C, Burdick JA, and Gerecht S (2011). Controlled activation of morphogenesis to generate a functional human microvasculature in a synthetic matrix. Blood 118, 804–815. [PubMed: 21527523]

Hanjaya-Putra D, Yee J, Ceci D, Truitt R, Yee D, and Gerecht S (2010). Vascular endothelial growth factor and substrate mechanics regulate in vitro tubulogenesis of endothelial progenitor cells. Journal of cellular and molecular medicine 14, 2436–2447. [PubMed: 19968735]

Hosseini A, Rasmi Y, Rahbarghazi R, Aramwit P, Daeihassani B, and Saboory E (2019). Curcumin modulates the angiogenic potential of human endothelial cells via FAK/P-38 MAPK signaling pathway. Gene 688, 7–12. [PubMed: 30472378]

Hozumi T, Kageyama T, Ohta S, Fukuda J, and Ito T (2018). Injectable hydrogel with slow degradability composed of gelatin and hyaluronic acid cross-linked by Schiff's base formation. Biomacromolecules 19, 288–297. [PubMed: 29284268]

Huebsch N, Arany PR, Mao AS, Shvartsman D, Ali OA, Bencherif SA, Rivera-Feliciano J, and Mooney DJ (2010). Harnessing traction-mediated manipulation of the cell/matrix interface to control stem-cell fate. Nature materials 9, 518. [PubMed: 20418863]

Humphries JD, Wang P, Streuli C, Geiger B, Humphries MJ, and Ballestrem C (2007). Vinculin controls focal adhesion formation by direct interactions with talin and actin. The Journal of cell biology 179, 1043–1057. [PubMed: 18056416]

Iruela-Arispe ML, and Davis GE (2009). Cellular and molecular mechanisms of vascular lumen formation. Developmental cell 16, 222–231. [PubMed: 19217424]

Jeon JS, Bersini S, Gilardi M, Dubini G, Charest JL, Moretti M, and Kamm RD (2015). Human 3D vascularized organotypic microfluidic assays to study breast cancer cell extravasation. Proceedings of the National Academy of Sciences 112, 214–219.

Kang H-W, Tabata Y, and Ikada Y (1999). Fabrication of porous gelatin scaffolds for tissue engineering. Biomaterials 20, 1339–1344. [PubMed: 10403052]

Kim SH, Kang JG, Kim CS, Ihm S-H, Choi MG, Yoo HJ, and Lee SJ (2014). The hsp70 inhibitor VER155008 induces paraptosis requiring de novo protein synthesis in anaplastic thyroid carcinoma cells. Biochemical and biophysical research communications 454, 36–41. [PubMed: 25450359]

Kovacs M, Toth J, Hetenyi C, Malnasi-Csizmadia A, and Sellers JR (2004). Mechanism of blebbistatin inhibition of myosin II. J Biol Chem 279, 35557–35563. [PubMed: 15205456]

Legant WR, Miller JS, Blakely BL, Cohen DM, Genin GM, and Chen CS (2010). Measurement of mechanical tractions exerted by cells in three-dimensional matrices. Nature methods 7, 969. [PubMed: 21076420]

Levental I, Georges PC, and Janmey PA (2007). Soft biological materials and their impact on cell function. Soft Matter 3, 299–306. [PubMed: 32900146]

Lewis DM, Pruitt H, Jain N, Ciccaglione M, McCaffery JM, Xia Z, Weber K, Eisinger-Mathason TK, and Gerecht S (2019). A feedback loop between hypoxia and matrix stress relaxation increases oxygen-Axis migration and metastasis in sarcoma. Cancer research 79, 1981–1995. [PubMed: 30777851]

Lewis DM, Tang V, Jain N, Isser A, Xia Z, and Gerecht S (2017). Collagen fiber architecture regulates hypoxic sarcoma cell migration. ACS Biomaterials Science & Engineering 4, 400–409.

Li S, Nih LR, Bachman H, Fei P, Li Y, Nam E, Dimatteo R, Carmichael ST, Barker TH, and Segura T (2017). Hydrogels with precisely controlled integrin activation dictate vascular patterning and permeability. Nature materials 16, 953. [PubMed: 28783156]

Liu Z, and Bilston L (2000). On the viscoelastic character of liver tissue: experiments and modelling of the linear behaviour. Biorheology 37, 191–201. [PubMed: 11026939]

Liu ZQ, Wei Z, Zhu XL, Huang GY, Xu F, Yang JH, Osada Y, Zrínyi M, Li JH, and Chen YM (2015). Dextran-based hydrogel formed by thiol-Michael addition reaction for 3D cell encapsulation. Colloids and Surfaces B: Biointerfaces 128, 140–148. [PubMed: 25744162]

Loebel C, Mauck RL, and Burdick JA (2019). Local nascent protein deposition and remodelling guide mesenchymal stromal cell mechanosensing and fate in three-dimensional hydrogels. Nature materials, 1.

Lou J, Stowers R, Nam S, Xia Y, and Chaudhuri O (2018). Stress relaxing hyaluronic acid-collagen hydrogels promote cell spreading, fiber remodeling, and focal adhesion formation in 3D cell culture. Biomaterials 154, 213–222. [PubMed: 29132046]

Madl CM, LeSavage BL, Dewi RE, Dinh CB, Stowers RS, Khariton M, Lampe KJ, Nguyen D, Chaudhuri O, and Enejder A (2017). Maintenance of neural progenitor cell stemness in 3D hydrogels requires matrix remodelling. Nature materials 16, 1233. [PubMed: 29115291]

Maia J, Ferreira L, Carvalho R, Ramos MA, and Gil MH (2005). Synthesis and characterization of new injectable and degradable dextran-based hydrogels. Polymer 46, 9604–9614.

Marchand M, Monnot C, Muller L, and Germain S (2019). Extracellular matrix scaffolding in angiogenesis and capillary homeostasis. Semin Cell Dev Biol 89, 147–156. [PubMed: 30165150]

Matsuoka S (1992). Relaxation phenomena in polymers (Hanser Munich etc.).

McCoy MG, Nyanyo D, Hung CK, Goerger JP, Zipfel WR, Williams RM, Nishimura N, and Fischbach C (2019). Endothelial cells promote 3D invasion of GBM by IL-8-dependent induction of cancer stem cell properties. Scientific reports 9, 9069. [PubMed: 31227783]

McCoy MG, Seo BR, Choi S, and Fischbach C (2016). Collagen I hydrogel microstructure and composition conjointly regulate vascular network formation. Acta biomaterialia 44, 200–208. [PubMed: 27545811]

McDonald SJ, Dooley PC, McDonald AC, Schuijers JA, Ward AR, and Grills BL (2009). Early fracture callus displays smooth muscle-like viscoelastic properties ex vivo: Implications for fracture healing. Journal of Orthopaedic Research 27, 1508–1513. [PubMed: 19472384]

McKinnon DD, Domaille DW, Cha JN, and Anseth KS (2014). Biophysically defined and cytocompatible covalently adaptable networks as viscoelastic 3D cell culture systems. Advanced materials 26, 865–872. [PubMed: 24127293]

Mofrad M, Golji J, Abdul Rahim N, and Kamm R (2004). Force-induced unfolding of the focal adhesion targeting domain and the influence of paxillin binding. Mech Chem Biosyst 1, 253–265. [PubMed: 16783922]

Moon JJ, Saik JE, Poche RA, Leslie-Barbick JE, Lee S-H, Smith AA, Dickinson ME, and West JL (2010). Biomimetic hydrogels with pro-angiogenic properties. Biomaterials 31, 3840–3847. [PubMed: 20185173]

Nam S, Stowers R, Lou J, Xia Y, and Chaudhuri O (2019). Varying PEG density to control stress relaxation in alginate-PEG hydrogels for 3D cell culture studies. Biomaterials 200, 15–24. [PubMed: 30743050]

Park KM, and Gerecht S (2014). Hypoxia-inducible hydrogels. Nature communications 5, 4075.

Pedrosa A-R, Bodrug N, Gomez-Escudero J, Carter EP, Reynolds LE, Georgiou PN, Fernandez I, Lees DM, Kostourou V, and Alexopoulou AN (2019). Tumor angiogenesis is differentially regulated by phosphorylation of endothelial cell focal adhesion kinase tyrosines-397 and-861. Cancer research, canres. 39342018.

Petit I, Jin D, and Rafii S (2007). The SDF-1-CXCR4 signaling pathway: a molecular hub modulating neo-angiogenesis. Trends Immunol 28, 299–307. [PubMed: 17560169]

Ren X-D, Kiosses WB, Sieg DJ, Otey CA, Schlaepfer DD, and Schwartz MA (2000). Focal adhesion kinase suppresses Rho activity to promote focal adhesion turnover. Journal of cell science 113, 3673–3678. [PubMed: 11017882]

Ronaldson-Bouchard K, and Vunjak-Novakovic G (2018). Organs-on-a-chip: a fast track for engineered human tissues in drug development. Cell stem cell 22, 310–324. [PubMed: 29499151]

Sacharidou A, Koh W, Stratman AN, Mayo AM, Fisher KE, and Davis GE (2010). Endothelial lumen signaling complexes control 3D matrix–specific tubulogenesis through interdependent Cdc42-and MT1-MMP–mediated events. Blood 115, 5259–5269. [PubMed: 20215637]

Shen Y-I, Abaci HE, Krupski Y, Weng L-C, Burdick JA, and Gerecht S (2014). Hyaluronic acid hydrogel stiffness and oxygen tension affect cancer cell fate and endothelial sprouting. Biomaterials science 2, 655–665. [PubMed: 24748963]

Shi Q, and Boettiger D (2003). A novel mode for integrin-mediated signaling: tethering is required for phosphorylation of FAK Y397. Molecular biology of the cell 14, 4306–4315. [PubMed: 12960434]

Stratman AN, Davis MJ, and Davis GE (2011). VEGF and FGF prime vascular tube morphogenesis and sprouting directed by hematopoietic stem cell cytokines. Blood 117, 3709–3719. [PubMed: 21239704]

Stratman AN, Saunders WB, Sacharidou A, Koh W, Fisher KE, Zawieja DC, Davis MJ, and Davis GE (2009). Endothelial cell lumen and vascular guidance tunnel formation requires MT1-MMP–dependent proteolysis in 3-dimensional collagen matrices. Blood 114, 237–247. [PubMed: 19339693]

Sun G, Shen YI, Ho CC, Kusuma S, and Gerecht S (2010). Functional groups affect physical and biological properties of dextran-based hydrogels. Journal of Biomedical Materials Research Part A: An Official Journal of The Society for Biomaterials, The Japanese Society for Biomaterials, and The Australian Society for Biomaterials and the Korean Society for Biomaterials 93, 1080–1090.

Swift J, Ivanovska IL, Buxboim A, Harada T, Dingal PDP, Pinter J, Pajerowski JD, Spinler KR, Shin J-W, and Tewari M (2013). Nuclear lamin-A scales with tissue stiffness and enhances matrix-directed differentiation. Science 341, 1240104. [PubMed: 23990565]

Tadokoro S, Shattil SJ, Eto K, Tai V, Liddington RC, de Pereda JM, Ginsberg MH, and Calderwood DA (2003). Talin binding to integrin ß tails: a final common step in integrin activation. Science 302, 103–106. [PubMed: 14526080]

Tang S, Ma H, Tu HC, Wang HR, Lin PC, and Anseth KS (2018). Adaptable Fast Relaxing Boronate-Based Hydrogels for Probing Cell–Matrix Interactions. Advanced Science 5, 1800638. [PubMed: 30250802]

Trappmann B, Gautrot JE, Connelly JT, Strange DG, Li Y, Oyen ML, Stuart MAC, Boehm H, Li B, and Vogel V (2012). Extracellular-matrix tethering regulates stem-cell fate. Nature materials 11, 642. [PubMed: 22635042]

Turturro MV, Christenson MC, Larson JC, Young DA, Brey EM, and Papavasiliou G (2013). MMP-sensitive PEG diacrylate hydrogels with spatial variations in matrix properties stimulate directional vascular sprout formation. PLoS One 8, e58897. [PubMed: 23554954]

Wang H, and Heilshorn SC (2015). Adaptable hydrogel networks with reversible linkages for tissue engineering. Advanced Materials 27, 3717–3736. [PubMed: 25989348]

Wang Y, and McNiven MA (2012). Invasive matrix degradation at focal adhesions occurs via protease recruitment by a FAK–p130Cas complex. J Cell Biol 196, 375–385. [PubMed: 22291036]

Wei Z, and Gerecht S (2018). A self-healing hydrogel as an injectable instructive carrier for cellular morphogenesis. Biomaterials 185, 86–96. [PubMed: 30236839]

Wei Z, Lewis DM, Xu Y, and Gerecht S (2017). Dual Cross-Linked Biofunctional and Self-Healing Networks to Generate User-Defined Modular Gradient Hydrogel Constructs. Advanced healthcare materials 6, 1700523.

Wei Z, Yang JH, Liu ZQ, Xu F, Zhou JX, Zrínyi M, Osada Y, and Chen YM (2015). Novel biocompatible polysaccharide-based self-healing hydrogel. Advanced Functional Materials 25, 1352–1359.

Wei Z, Yang JH, Zhou J, Xu F, Zrínyi M, Dussault PH, Osada Y, and Chen YM (2014). Self-healing gels based on constitutional dynamic chemistry and their potential applications. Chemical Society Reviews 43, 8114–8131. [PubMed: 25144925]

Wojtecki RJ, Meador MA, and Rowan SJ (2011). Using the dynamic bond to access macroscopically responsive structurally dynamic polymers. Nature materials 10, 14. [PubMed: 21157495]

Yamaguchi J, Kusano KF, Masuo O, Kawamoto A, Silver M, Murasawa S, Bosch-Marce M, Masuda H, Losordo DW, Isner JM, et al. (2003). Stromal cell-derived factor-1 effects on ex vivo expanded endothelial progenitor cell recruitment for ischemic neovascularization. Circulation 107, 1322–1328. [PubMed: 12628955]

Yoon C, Choi C, Stapleton S, Mirabella T, Howes C, Dong L, King J, Yang J, Oberai A, and Eyckmans J (2019). Myosin IIA–mediated forces regulate multicellular integrity during vascular sprouting. Molecular biology of the cell 30, 1974–1984. [PubMed: 31318321]

Yu CH, Law JB, Suryana M, Low HY, and Sheetz MP (2011). Early integrin binding to Arg-Gly-Asp peptide activates actin polymerization and contractile movement that stimulates outward translocation. Proc Natl Acad Sci U S A 108, 20585–20590. [PubMed: 22139375]

Zhang B, Montgomery M, Chamberlain MD, Ogawa S, Korolj A, Pahnke A, Wells LA, Massé S, Kim J, and Reis L (2016). Biodegradable scaffold with built-in vasculature for organ-on-a-chip engineering and direct surgical anastomosis. Nature materials 15, 669. [PubMed: 26950595]

Zhao X, Liu S, Yildirimer L, Zhao H, Ding R, Wang H, Cui W, and Weitz D (2016). Injectable stem cell-laden photocrosslinkable microspheres fabricated using microfluidics for rapid generation of osteogenic tissue constructs. Advanced Functional Materials 26, 2809–2819.

Zheng Y, Chen J, Craven M, Choi NW, Totorica S, Diaz-Santana A, Kermani P, Hempstead B, Fischbach-Teschl C, and López JA (2012). In vitro microvessels for the study of angiogenesis and thrombosis. Proceedings of the national academy of sciences 109, 9342–9347.

Ziegler WH, Gingras AR, Critchley DR, and Emsley J (2008). Integrin connections to the cytoskeleton through talin and vinculin (Portland Press Ltd.).

Highlights

- Development of dynamic hydrogels to study matrix dynamics role in vascular assembly
- Dynamic hydrogels promote cell contractility-mediated integrin clustering
- Non-dynamic hydrogels prevent integrin clustering, subsequently inhibit morphogenesis
- Dynamic hydrogels promote the formation of microvessels and angiogenesis in vivo.

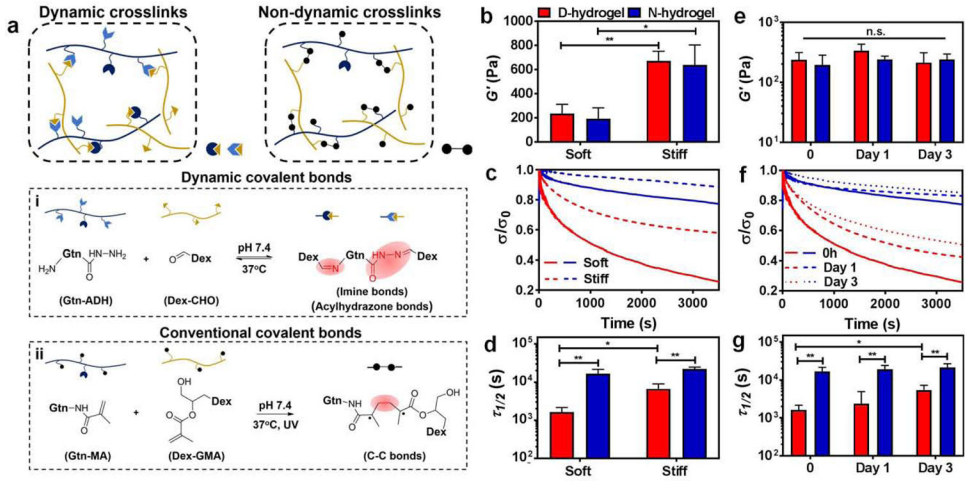

Figure. 1. Design and characterization of Dynamic-network hydrogels (D-hydrogels) and Non-dynamic-network hydrogels (N-hydrogels).

See also Figure S1. (a) Schematic depicting networks of D-hydrogel cross-linked by the dynamic covalent bonds of imine and acylhydrazone bonds between Gtn-ADH and Dex-CHO, and N-hydrogel cross-linked by the covalent bonds between Gtn-MA and Dex-GMA. (b) Storage moduli (*G'*) of D-hydrogels and N-hydrogels with different stiffness. (D-hydrogels are in red and N-hydrogels are in blue) (c) Stress relaxation curves of D-hydrogels and N-hydrogels with different stiffness. Stress is normalized to the initial stress. (d) Quantification of timescale at which the stress is relaxed to half its original value, $T_{1/2}$, from stress relaxation tests of D-hydrogels and N-hydrogels with differing stiffness. (e) No significant change in stiffness, *G'*, of D-hydrogels and N-hydrogel along 3 days of incubation in endothelial growth medium-2 (EGM-2). (f) Significant increase in stress relaxation time over 3 days in culture in EGM-2 but (g) half stress relax time, $T_{1/2}$, is maintained lower than in N-hydrogel along the 3 days culture period. Significance levels were set at n.s. $p > 0.05$, $*p \leq 0.05$, and $**p \leq 0.01$.

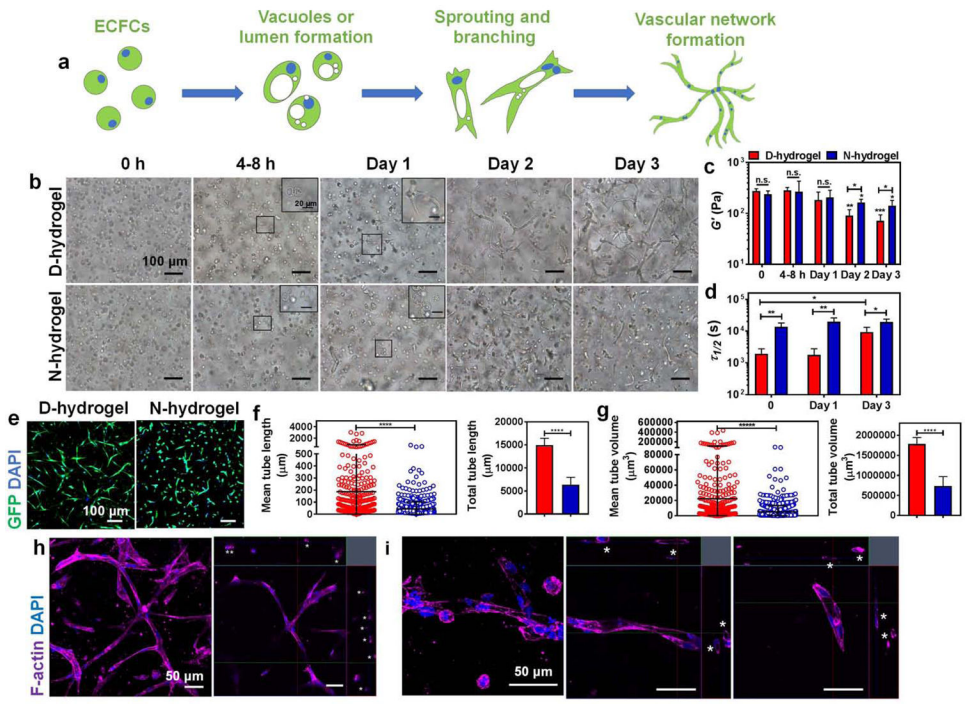

Figure. 2. Hydrogels with dynamic and non-dynamic networks differently modulate morphogenesis of encapsulated endothelial colony forming cells (ECFCs).

See also Figures S2 and S3. (a) Schematic displaying the vasculogenesis of ECFCs encapsulated in hydrogels: from initial step of vacuole or lumen formation, then to sprouting and branching, to final tubulogenesis of complex vascular bed. (b) Light micrographic images showing phenotype changes of encapsulated ECFCs in D-hydrogels and N-hydrogels along 3 days in culture in EGM-2 media. Scale bars are 100 μm for the larger images and 20 μm for the insets. (c) The stiffness, *G'*, and (d) $T_{1/2}$ of D-hydrogels and N-hydrogels encapsulated with ECFCs along the 3 days culture period. D-hydrogels are in red and N-hydrogels are in blue) (e) Confocal maximum intensity projection images of vascular phenotypes in D-hydrogels and N-hydrogels after 3 days in culture (GFP-ECFC in green, nuclei in blue) showing extensive vascular bed formed in D-hydrogels. Scale bars are 100 μm. (f-g) Quantitative analysis of vascular tube formation after 3 days in culture shows higher mean and total tube length (f), and higher mean and total tube volume (g) of ECFCs encapsulated in D-hydrogels compared with N-hydrogels (analysis using Imaris Filament Tracer; N = 3 biological replicates with 5–6 images per replicate). (h) Representative confocal maximum intensity projection with orthogonal views (on the upper and right side of the images) of luminal structures (indicated with asterisks) in D-hydrogels after 3 days in culture (F-actin in purple and nuclei in blue). Scale bars are 50 μm. (i) Magnified confocal maximum intensity projection images of vessels with orthogonal views (on the upper and right side of the two images of the left) of luminal structures (indicated with asterisks) in D-hydrogels after 3 days in culture (F-actin in purple and nuclei in blue). Scale bars are 50 μm. Significance levels were set at n.s. $p > 0.05$, *$p \leq 0.05$, **$p \leq 0.01$, and ****$p \leq 0.0001$.

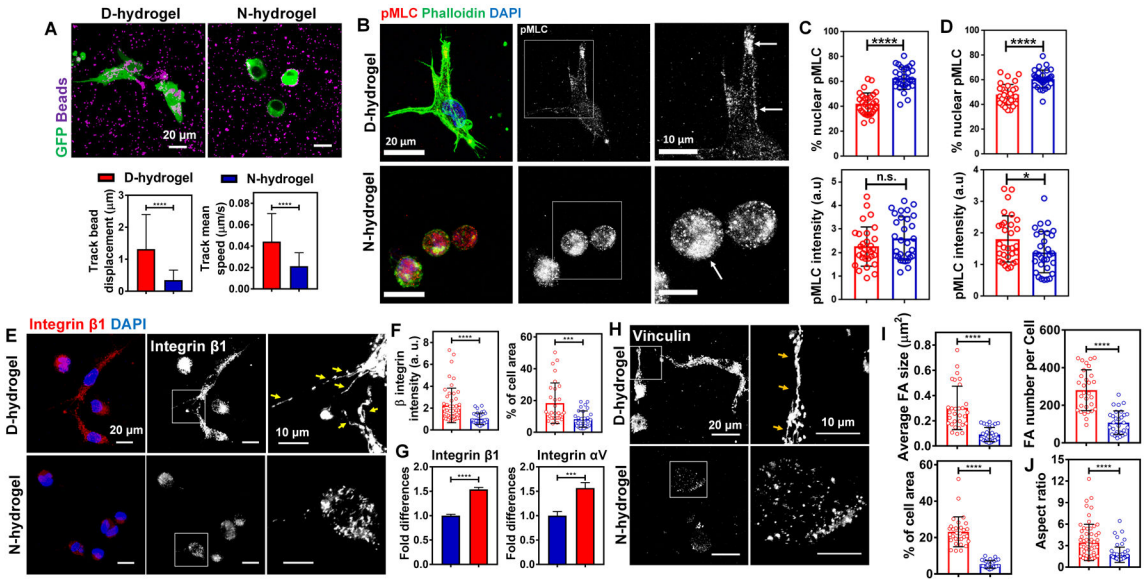

Fig. 3. Hydrogels with dynamic networks promote focal adhesion (FA) formation in encapsulated ECFCs.

See also Figure S4. (a) Representative IF images of ECFCs (in green) with fluorescent beads (in purple) in D-hydrogels and N-hydrogels, and quantification of displacement and speed of the beads over time lapse (n = 15 cells from biological triplicates). (D-hydrogels are in red and N-hydrogels are in blue). Scale bars are 20 μm (b) Maximum intensity projections of confocal images of cells 12h after embedding into N- and D-hydrogels show protrusion formation and localization of pMLC to actin in D-hydrogels. Cells embedded in N-hydrogels have round shape without any protrusions and pMLC localized to the nucleus (phalloidin in green, pMLC in red, DAPI in blue). Scale bars are 20 μm. (c) corresponding quantification (n=30 cells from biological triplicates) of normalized intensities (lower graph) and % nuclear protein to overall protein levels (upper graph). (d) Quantification of normalized intensities (lower graph) and % nuclear protein to overall protein levels (upper graph) of cells embedded into D- and N-hydrogels after 24 h in culture. (e) IF images of integrin β1 staining and (f) corresponding quantifications (n = 30 cells from biological triplicates) of the normalized intensities (left graph) and FA areas (calculated as a percentage of the total cell area; right graph) showing more FA in ECFCs encapsulated within D-hydrogels compared to N-hydrogels, after day 1 in culture. Scale bars are 20 μm and 10 μm for higher magnification of FA. (g) Real-time RT-PCR analysis show higher integrin β1 and integrin αV mRNA expression in ECFCs encapsulated in D-hydrogels compared with N-hydrogels after day 1 in culture. (h) IF images of GFP-ECFCs encapsulated in D-hydrogels and N-hydrogels stained for vinculin after day 1 in culture. Scale bar is 20 μm and 10 μm for higher magnification of FA. (i) Quantifications (n = 30 cells from biological triplicates) of FA size, number and areas using vinculin staining showing more FA in ECFCs encapsulated in D-hydrogels compared with N-hydrogels after day 1 in culture. (j) Quantifications (n = 60 cells from biological triplicates) of aspect ratio using F-actin staining, demonstrating ECFCs spreading to a higher degree when encapsulated in D-hydrogels compared with N-hydrogels after 1 day in culture. Significance levels were set at ***$p \leq 0.001$ and ****$p \leq 0.0001$.

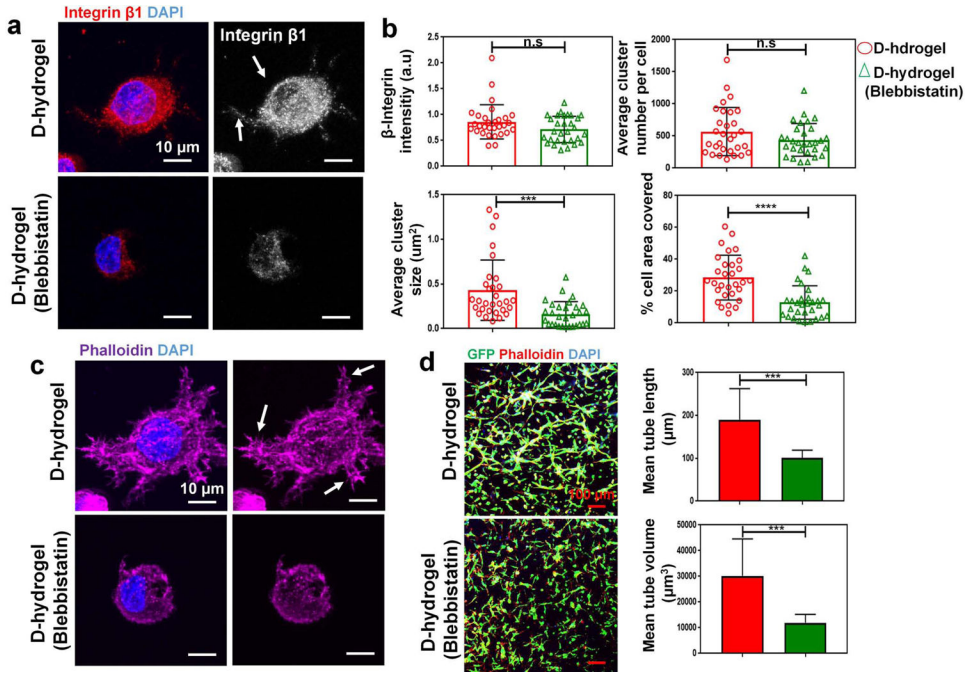

Fig. 4. Cell contraction mediates integrin clustering and subsequent vessel formation.

Inhibition of cell contractility with Blebbistatin leads to reduction in integrin cluster size. (a) Maximum intensity projections of confocal images show reduced integrin cluster size and area coverage in cells treated with 60 μm blebbistatin after 24 hrs in culture. (integrin β1 in red, nuclei in blue). Scale bars are 10 μm. (b) analysis of integrin cluster size, number per cell, are covered and relative intensity (n = 30 cells from biological triplicates) of the normalized intensities (top left graph) and integrin area (calculated as a percentage of the total cell area; bottom right graph) showing smaller integrin clusters in ECFCs encapsulated within D-hydrogels treated with blebbistatin for 24 hrs. (c) Maximum intensity projections of representative confocal image of reduced lamellipodial extension in ECFCs in D-hydrogels treated with blebbistatin for 24 hrs (nuclei blue, phalloidin magenta). Scale bare 10 μm. (d) Confocal projection images of day 3 (GFP-ECFC in green, nuclei in blue and phalloidin in red), showing inhibition of vasculature formation in blebbistatin treated cells compared to untreated controls. Scale bars are 100 μm. Quantitative analysis of vascular tube formation, in D-hydrogels and D-hydrogels treated with blebbistatin after 3 days showing a decrease in mean tube length, as well as mean and tube volume (analysis using Imaris Filament Tracer; N = 3 biological replicates with 4 images per replicate). Significance levels were set at ***$p \leq 0.001$ and ****$p \leq 0.0001$.

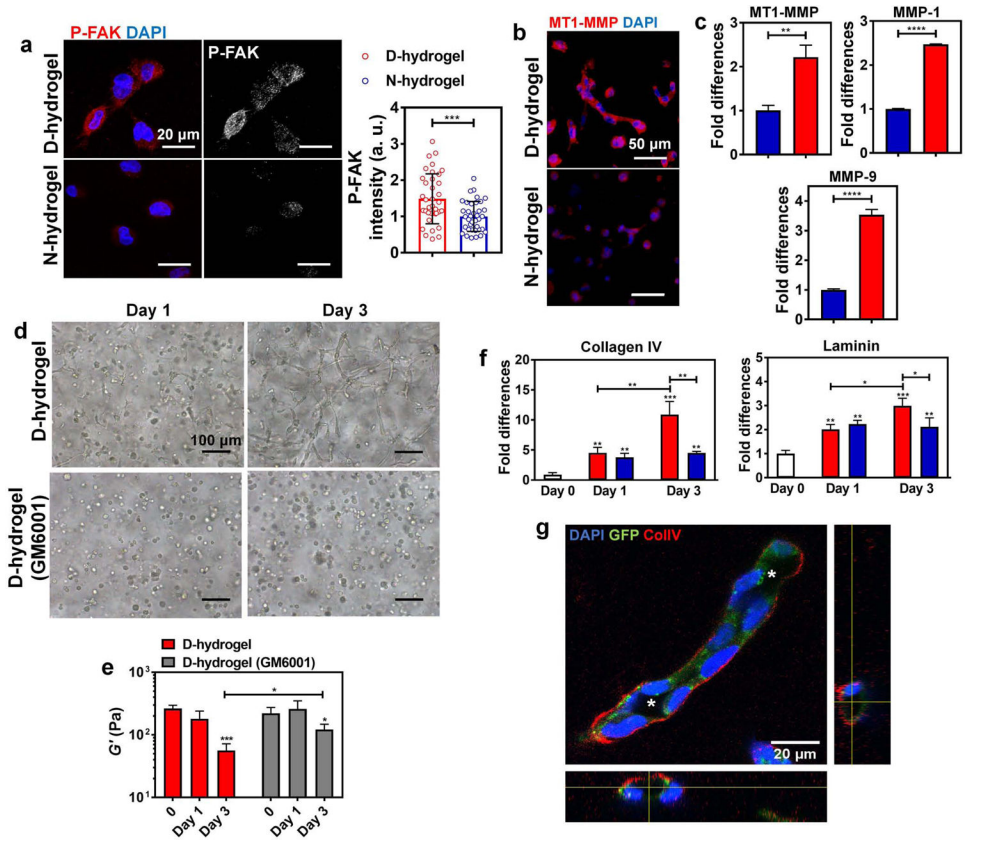

Fig. 5. Dynamic networks lead to the activation of FAK, matrix degradation via increased MMP expression and ECM deposition.

See also Figure S5. (a) Representative IF images and quantifications of the normalized intensities of P-FAK showing increased activation in ECFCs encapsulated in D-hydrogels compared to N-hydrogels (P-FAK in red, nuclei in blue) (n = 30 cells from biological triplicates). Scale bars are 20 μm. (b) Representative IF images of MT1-MMP stains showing higher expression of MT1-MMP in ECFCs encapsulated in D-hydrogels compared to N-hydrogels after 24 hrs in culture (MT1-MMP in red, nuclei in blue). Scale bars are 50 μm. (c) Real-time RT-PCR analysis show that ECFCs encapsulated in D-hydrogels highly express MT1-MMP, MMP-1 and MMP-9 mRNA compared to N-hydrogels. (D-hydrogels are in red and N-hydrogels are in blue) (d) Light micrographic images of ECFCs encapsulated in D-hydrogels treated with MMP inhibitor GM6001, at a concentration of 0.1 mM after days 1 and 3 of culture, showing inhibition of sprouting and vasculature formation compared to untreated controls. Scale bars are 100 μm (e) The *G'* of ECFC-loaded D-hydrogel controls and D-hydrogels treated with GM6001 along with 3 days culture period. (f) Real-time RT-PCR analysis show that ECFCs encapsulated in D-hydrogels highly express Collagen IV and laminin on day 3 of culture compared to N-hydrogels. (g) Representative confocal maximum intensity projection with orthogonal views (on the bottom and right side of the image) of ColIV stains (in white/red; cells in green; nuclei in blue) after 3 days in D-hydrogels show strong localization of ColIV at the basement membrane of the lumenized vessels. Lumens are indicated with an asterisk. Scale bars are 20 μm. For graphs: D-hydrogels are in red, D-hydrogels treated with GM6001 or cells before

encapsulation are in grey. Significance levels were set at *$p \leq 0.05$, **$p \leq 0.01$, ***$p \leq 0.001$ and ****$p \leq 0.0001$.

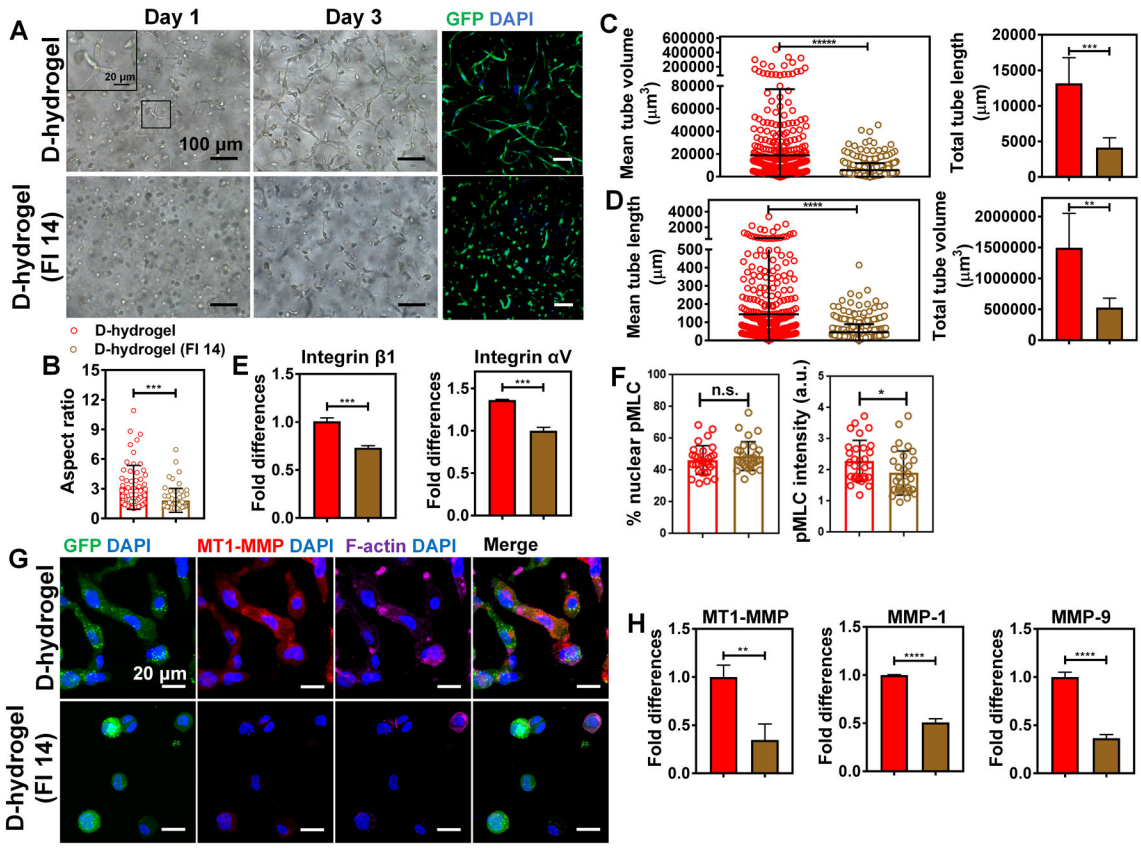

Fig. 6. FAK activation in ECFCs is required for D-hydrogel remodeling and vascular morphogenesis.

See also Figure S5. (a) Light micrographic images of ECFCs encapsulated within D-hydrogels treated with FAK inhibitor 14 (FI 14) at a concentration of 10 μM after days 1 and 3 of culture and corresponding confocal projection images of day 3 (GFP-ECFC in green, nuclei in blue), showing inhibition of sprouting and vessel formation compared to untreated controls. Scale bars are 100 μm and 20 μm for the inset. (b) Quantifications of ECFC aspect ratio showing cell spreading is reduced when encapsulated in D-hydrogels treated with FI 14 compared with control D-hydrogels, after 24 hrs in culture (n = 60 cells from biological triplicates). (D-hydrogels are in red and D-hydrogels treated with FI 14 are in brown). (c) Quantitative analysis of vascular tube formation in D-hydrogels and D-hydrogels treated with FI 14 after 3 days showing a decrease in mean and total tube length as well as (d) mean and total tube volume (analysis using Imaris Filament Tracer; N = 3 biological replicates with 5–6 images per replicate). (e) RT-PCR analysis shows downregulation of integrin β1 and integrin αV mRNA expression in ECFCs in D-hydrogels treated with FI 14 compared to D-hydrogel controls after 24 hrs in culture. Significance levels were set at $^{**}p \leq 0.01$, $^{***}p \leq 0.001$ and $^{****}p \leq 0.0001$. (f) Quantification of normalized intensities (right graph) and % nuclear protein to overall protein levels (left graph) of cells embedded into D-hydrogels and treated with 10 μm FAK inhibitor. (g) Representative IF images show lower expression for MT1-MMP in ECFCs encapsulated in D-hydrogels treated with FI 14 compared to control D-hydrogels after 24 hrs in culture (GFP in green, MT1-MMP in red, phalloidin in purple and nuclei in blue). Scale bar are 20 μm. (h) RT-PCR analysis shows downregulation of

MT1-MMP, MMP-1 and MMP-9 mRNA expression in ECFCs encapsulated in D-hydrogels treated with FI 14 compared to D-hydrogel controls after 24 hrs in culture.

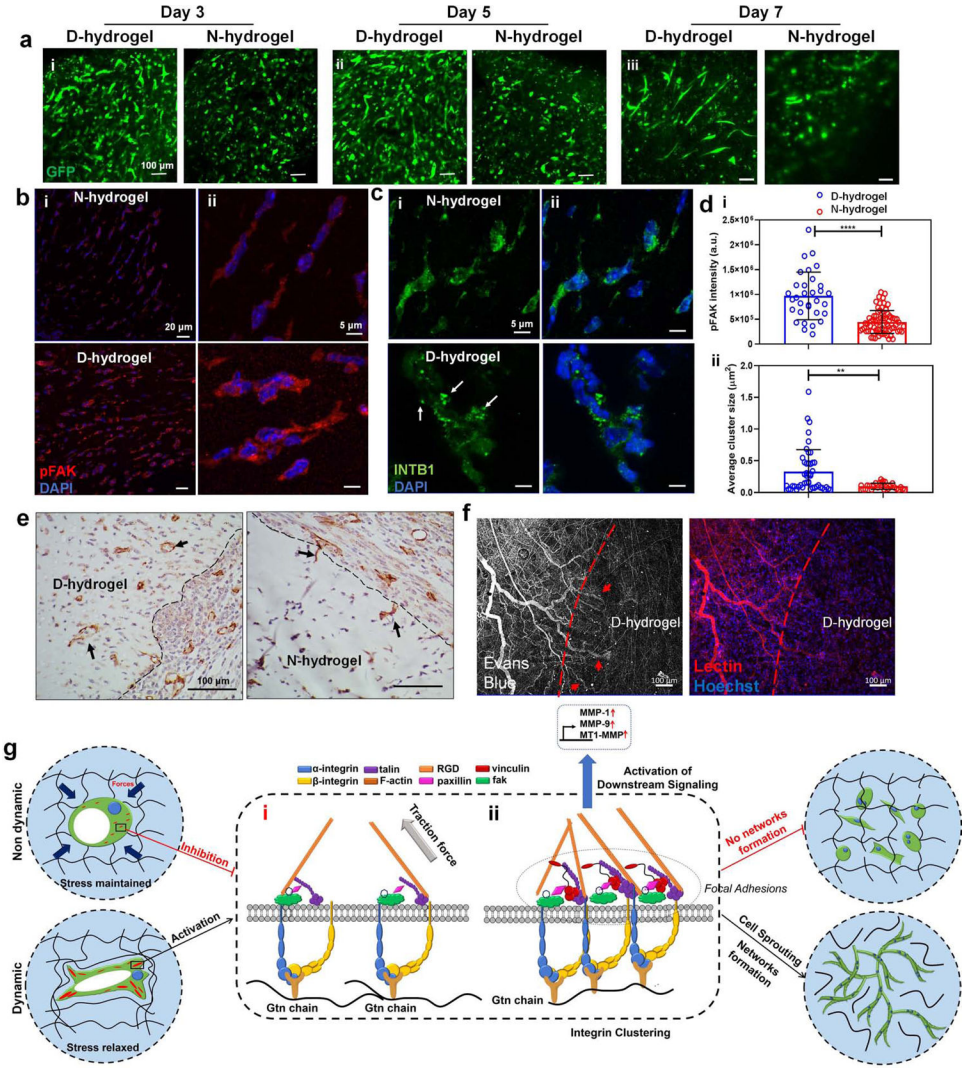

Fig. 7. Dynamic networks accelerate vasculogenesis *in vivo* and proposed molecular pathway of ECFCs in response to dynamic networks.

See also Figures S6 and S7. (a) GFP-ECFC-loaded D- and N-hydrogels were directly implanted subcutaneously in nude mice and retrieved after (i) day 3, (ii) day 5, and (iii) day 7 (n = 3). Representative confocal images show GFP-ECFC (in green) of the corresponding extracted hydrogels. (b) FAK activation is increased in ECFC-loaded D-hydrogels compared with N-hydrogels *in vivo* on day 5 indicated by pFAK signal intensity (pFAK in red, nuclei in blue) scale bars are 20 μm (i) and 5 μm (ii) (c) integrin cluster size is larger in ECFC-loaded D-hydrogels (β1-integrin in green some indicated by arrows, nuclei in blue) *in vivo* on day 5 scale bars are 20 μm (i) and 5 μm (ii). (d) quantification of pFAK signal intensity (i) and β1-integrin cluster size. (e) Representative histological images of CD31+ vessels infiltrating into acellular hydrogels in D-hydrogels compared to individual cells invading into the edge of N-hydrogels (indicated by arrows). Scale bars are 100 μm (f) Vessels, labeled with lectin, infiltrating into D-hydrogels were perfused (indicated by arrows) with Evans blue dye injected intravenously. Scale bars are 100 μm. Significance levels were set at $^{**}p \leq 0.01$, $^{***}p \leq 0.001$ and $^{****}p \leq 0.0001$. (g) Hydrogels with dynamic networks enable

the rapid formation of FA in a stiffness-independent manner. Contrarily, static covalent hydrogels do not facilitate the formation of FA, leading to an abrogation of vascular morphogenesis. In both systems, ECFCs interact with the hydrogel binding sites, leading to vacuole and lumen formation. (i) The rigidity of the non dynamic matrix prevents the formation of integrin clusters via cell contractility inhibition; (ii) In the dynamic matrix, integrin β1 interaction with RGD binding sites of the Gtn leads to the recruitment of FAK and other FA proteins. In a second step, pMLC mediated actin contractility leads to the formation of larger integrin clusters. Integrin clustering and the recruitment of vinculin to the FAs leads to the formation of larger, stable FAs. These FAs allow for robust downstream signaling and further FAK activation. Activated FAK then further contributes to cell contraction and integrin expression promoting the formation of larger integrin clusters and taking in part in robust downstream signaling. The activation of FAK leads to the upregulation of the MT1-MMP and MMP-1, MMP-9, resulting in matrix degradation and remodeling, allowing the progression of ECFC vasculogenesis.

KEY RESOURCES TABLE

REAGENT or RESOURCE	SOURCE	IDENTIFIER
Antibodies		
Rabbit monoclonal anti-Cdc42 (clone 11A11)	Cell Signaling Technology	Cat#2466, RRID: AB_2078082
Mouse monoclonal anti- Integrin β1 (clone 4B7R)	Santa Cruz Biotechnology	Cat#Sc-9970, RRID:AB_627004
Mouse monoclonal anti-Vinculin	Sigma-Aldrich	Cat#v9131, RRID: AB_477629
Rabbit polyclonal anti-phospho-FAK (Tyr397)	Thermo Fisher Scientific	Cat#44-624G, RRID: AB_2533701
Rabbit monoclonal anti-MMP14 (clone EP1264Y)	abcam	Cat#ab51074, RRID: AB_881234
Rabbit polyclonal anti-YAP (clone H-125)	Santa Cruz Biotechnology	Cat#Sc-15407, RRID: AB_2273277
Rabbit polyclonal anti-ColIV	abcam	Cat# ab6586, RRID: AB_305584
Rabbit polyclonal anti-human CD31	abcam	Cat# ab32457, RRID: AB_726369
Rabbit polyclonal anti-CD31	abcam	Cat# ab28364, RRID: AB_726362
Rabbit polyclonal anti-pMLC	Cell Signaling Technology	Cat# 3674, RRID:AB_2147464
Donkey anti-mouse IgG secondary antibody- Alexa Fluor 546 conjugate	Invitrogen	Cat# A10036, RRID: AB_2534012
Goat anti-mouse IgG Secondary Antibody Alexa Fluor 488 conjugate	Invitrogen	Cat#A11029, RRID: AB_138404
Goat anti-rabbit IgG Secondary Antibody Alexa Fluor 488 conjugate	Invitrogen	Cat#A11008, RRID: AB_143165
Goat anti-rabbit IgG Secondary Antibody Alexa Fluor 546	Invitrogen	Cat#11035, RRID: AB_143051
Alexa Fluor 635-phalloidin	Invitrogen	Cat#A34054
Alexa Fluor 488- phalloidin	Invitrogen	Cat#A12379
Chemicals, Peptides, and Recombinant Proteins		
Gelatin Type A	Sigma-Aldrich	CAS: 9000-70-8; Cat#V900863-100G
Adipic acid dihydrazide	Sigma-Aldrich	CAS: 1071-93-8; Cat#A0638-25G
1-Hydroxybenzotriazole hydrate	Sigma-Aldrich	CAS: 123333-53-9; Cat#711489-50G
N-(3-Dimethylaminopropyl)-N’-ethylcarbodiimide hydrochloride	Sigma-Aldrich	CAS: 25952-53-8; Cat#8009070025
Dextran (Mn = 110,000)	Sigma-Aldrich	CAS: 9004-54-0
Sodium periodate	Sigma-Aldrich	CAS: 7790-28-5; Cat#S1878-25G
tert-Butylcarbazate	Sigma-Aldrich	CAS: 870-46-2; Cat#B91005-5G
Methacrylic anhydride	Sigma-Aldrich	CAS: 760-93-0; Cat#276685-100ML
4-Dimethylaminopyridine	Sigma-Aldrich	CAS: 1122-58-3; Cat#107700-25G
Glycidyl methacrylate	Sigma-Aldrich	CAS: 106-91-2; Cat#151238-100G
2-Hydroxy-4’-(2-hydroxyethoxy)-2-methylpropiophenone	Sigma-Aldrich	CAS: 106797-53-9; Cat#410896-10G
Evans Blue dye	Sigma-Aldrich	CAS: 314-13-6; Cat#E2129-10G
Rhodamine B	Sigma-Aldrich	CAS: 81-88-9; Cat#R6626-25G
DAPI (4’,6-Diamidino-2-Phenylindole, Dihydrochloride)	ThermoFisher Scientific	Cat# D1306
VEGF	R&D Systems	Cat#293-VE-010
bFGF	R&D Systems	Cat#233-FB-010
Endothelial growth media-2	Lonza	CC-3162

REAGENT or RESOURCE	SOURCE	IDENTIFIER
FBS (Defined)	Hyclone	Cat# SH30070.03
GM6001 MMP inhibitor	Sigma-Aldrich	Cat#CC1010
Fak inhibitor 14	Sigma-Aldrich	CAS: 4506-66-5; Cat#SML0837-10MG
DMSO	Sigma-Aldrich	Cat#D2438-10ML
Paraformaldehyde (PFA)	Sigma-Aldrich	Cat# 003218
Antibody diluent solution	Life Technologies	Cat# 003218
Triton X-100	Sigma-Aldrich	Cat#T8787
Trypsin-EDTA (0.05%)	ThermoFisher Scientific	Cat#25300054
Blebbistatin	Sigma-Aldrich	B0560
Collagen type I	BD Biosciences, Franklin Lakes, NJ	Cat#354236
Critical Commercial Assays		
WSE-1 assay	Roche	Cat# 05015944001
FluoSpheres	ThermoFisher Scientific	Cat# F8816
TaqMan™ Gene Expression Master Mix Thermo Fisher Scientific Cat#4369016	ThermoFisher Scientific	Cat#4369016
ImmPRESS HRP anti-rabbit IgG polymer detection kit	Vector Laboratories	Cat# MP-7401, RRID:AB_2336529
Experimental Models: Cell Lines		
Primary human: Passage 6–9 ECFCs	M. Yoder; Indiana University Yoder et al., 2007	N/A
Primary human: Passage 6–9 GFP-ECFCs	Transfected by K. Eisinger; University of Pennsylvania	N/A
Experimental Models: Organisms/Strains		
Mouse: 7–8 weeks old female nude mice Crl:NU-*Foxn1*^{nu} Immunodeficient Outbred	Charles River	Cat# CRL:088, RRID:IMSR_CRL:088
Mouse: 6–8 weeks old male C57BL/6 mice	The Jackson Laboratory	Cat# 5816320, RRID:MGI:5816320
Oligonucleotides		
MMP14 (hs01037003_g1)	Thermo Fisher Scientific	Cat# 4453320
MMP1 (hs00233958_m1)	Thermo Fisher Scientific	Cat# 4453320
MMP9 (hs00957562_m1)	Thermo Fisher Scientific	Cat# 4453320
ITGAV (hs00233808_m1)	Thermo Fisher Scientific	Cat# 4453320
ITGB1 (hs00559595_m1)	Thermo Fisher Scientific	Cat# 4453320
LAMC1 (hs00267056_m1)	Thermo Fisher Scientific	Cat# 4453320
COL4A1 (hs00266237_m1)	Thermo Fisher Scientific	Cat# 4453320
Software and Algorithms		
ImageJ	Schneider et al., 2012	ImageJ, RRID:SCR_003070
Imaris version 9.0	Bitplane	Imaris, RRID:SCR_007370
MATLAB script	MathWorks	MATLAB, RRID:SCR_001622
Prism version 7.04	GraphPad Software Inc.	PRISM, RRID:SCR_005375
ZEN imaging software	Carl Zeiss	Black Zen software, RRID:SCR_018163